On the Geometric and Statistical Signature of Landscape Forming Processes

A DISSERTATION
SUBMITTED TO THE FACULTY OF THE GRADUATE SCHOOL
OF THE UNIVERSITY OF MINNESOTA
BY

Paola Passalacqua

IN PARTIAL FULFILLMENT OF THE REQUIREMENTS
FOR THE DEGREE OF
Doctor Of Philosophy

December, 2009

© Paola Passalacqua 2009
ALL RIGHTS RESERVED

Acknowledgements

I would like to thank Efi Foufoula-Georgiou, my adviser, for helping me and supporting me during these years. I really enjoyed working with her, her approach to problems and her interest shaped my thinking.

I would also like to express my sincere gratitude to the members of my committee, Heinz Stefan, Christopher Paola, Vaughan Voller and Andrea Rinaldo for their invaluable suggestions and comments.

I am indebted to Guillermo Sapiro, Bill Dietrich, Paolo Tarolli, Patrick Belmont, Tien Do Trung and Vamsi Ganti, for the stimulating and fruitful collaborations.

I thank the members of my research group, past and present, for help, encouragement and provoking discussions.

I greatly appreciated the financial support of the National Center for Earth-Surface Dynamics (NCED), National Science Foundation (NSF), the Edward Silberman Fellowship and Minnesota Supercomputing Institute (MSI).

My family and friends receive my warmest appreciation for their support during these years.

Abstract

The physical processes that shape landscapes are complex and involve the interaction of water, soil, vegetation and biota over a range of scales. Yet, as complex as these interactions may seem to be, the landscapes we see around us often exhibit striking hierarchical order and geometric/statistical properties that are subject to scale renormalization. The overall goal of this research is to contribute to the theoretical foundation of extracting geomorphic features of interest from high resolution topography and use the extracted features for process understanding and for advancing landscape evolution modeling.

Specifically, an advanced methodology for geomorphic feature extraction is developed and implemented on several high resolution data sets of different characteristics, from a steep and landslide-dissected basin, to a mountainous region, to a flat and partly artificially drained area. This new methodology incorporates nonlinear diffusion for the pre-processing of the data, both to focus the analysis on the scales of interest and to enhance features that are critical to the network extraction. Following this pre-processing, channels are defined as curves of minimal effort, or geodesics, where the effort is measured based on fundamental geomorphological characteristics such as flow accumulation and iso-height contours curvature. The developed channel network extraction methodology is compared in terms of performance to a previously proposed channel extraction methodology based on wavelets. The results show that the geometric nonlinear framework is more computationally efficient and achieves better localization and robust extraction of features, especially in areas where gentle slopes prevail. The automatic extraction of channel morphology, such as cross-section, banks location, water surface elevation, is also addressed, as well as the possibility of distinguishing the signature of natural features such as channels from the one of artificial features, such as drainage ditches.

One motivation for extracting detailed geomorphic features from landscapes is the premise that this will lead to improved process understanding (e.g., by relating the observed form to physical processes that gave rise to that form) and improved modeling (e.g., incorporate important localized features in hydrologic or sediment transport models or develop sophisticated metrics for testing the performance of landscape evolution

models). With this premise in mind, work herein presents preliminary results along a particular new direction related to geomorphic transport laws and landscape evolution modeling. Specifically, motivated by: (a) our experience that geomorphic attributes, such as slope and curvature, are scale-dependent and thus the resulting sediment flux computed from the typical transport laws would also be scale-dependent, and (b) that landscapes present heterogeneity over a large range of scales, we put forward the idea of a non-local sediment flux formulation to be explored in landscape evolution modeling. Along these lines, a simple landscape evolution model is proposed and its ability to reproduce some common statistical properties of real landscapes is examined.

Contents

List of Figures

Chapter 1

Introduction

The study of landscapes and of the geomorphic transport laws that can explain their variability and shape, has been the subject of research for many years. Starting with the work of Culling [3], which used a linear diffusion model of slope erosion, several landscape evolution models have been proposed, becoming a common approach for studying a wide range of problems [4, 5, 6, 7, 8, 9, 10, 11, 12, 13, 14, 15, 16, 17, 18, 19, 20, 21, 22]. Dietrich et al. [23] defined a geomorphic transport law as a mathematical expression of mass flux or erosion caused by one or more processes acting over geomorphologically significant spatial and temporal scales. This 'law' might not always be derivable from first principles, but only needs to summarize the physical processes operating on landscapes. Geomorphic transport laws are far from being understood despite their extensive use. Furthermore, simple laws typically used, e.g., linear or nonlinear diffusion, suffer from scale-dependency of their parameters in order to properly account for subgrid-scale variability (e.g.,[24, 25]).

To better understand geomorphic transport laws and inform landscape evolution models, detailed analysis of real landscapes is needed in order to quantify their geometrical and statistical properties and compare them to those predicted by the models. The recent availability of LiDAR high resolution data sets (resolution ranging between 0.5 and 3 meters) has opened up new opportunities, and new challenges, for the detailed quantification of geomorphic features from digital elevation data. Features of interest include hillslope shapes, channel head locations, type and location of earth flows and landslides, channel banks and floodplains, terraces, bluffs, ravines, etc., all important

elements of a sediment and landscape evolution modeling framework and also for understanding the physical processes that gave rise to a certain landscape.

Recently several studies have explored the use of LiDAR data for a suite of applications, such as channel network extraction [26]; landslide identification [27, 28, 29, 30, 31]; detecting channel head locations [31]; geomorphological mapping of glacial landforms [32]; recognition of depositional features of alluvial fans [33, 34, 35] and channel bed morphology [36]; as well as calculation of slope for headwater channel network analysis [37].

The goal of this research is to contribute to the theoretical foundation of extracting geomorphic features of interest from high resolution topography and use the extracted features for process understanding and for advancing landscape evolution modeling. Specifically, the objectives of this research are:

1. Developing the next generation of mathematical algorithms able to detect geomorphic features from LiDAR data via the concepts of space-scale filtering and geometric optimization;

2. Evaluating these methodologies over a suite of terrains ranging from steep soil-mantled landscapes, to flat areas and to geologically heterogeneous landscapes;

3. Exploring a new geomorphic transport law, based on the hypothesis of non-local sediment flux, in reproducing attributes of real landscapes and thus proposing the investigation of an alternative class of landscape evolution models.

The organization of the thesis is as follows. In Chapter 2 we give some mathematical background on wavelets, nonlinear filtering, geodesic curves, and a wavelet-based methodology for channel network extraction. Chapter 3 presents in detail the developed geomorphic feature extraction methodology based on nonlinear space-scale filtering and geodesic optimization. In this chapter we also present its first application to a steep and landslide dissected basin, the Skunk Creek basin, located in Northern California and part of the Eel River basin. In Chapter 4 we compare the performance of the wavelet-based methodology developed by Lashermes et al. [26] and the geometric nonlinear methodology developed herein in part of the Cordon basin, a mountainous landscape located in the Italian Alps. In Chapter 5 we explore the challenges and opportunities

presented by the geomorphic feature extraction in flat terrains. In this chapter we also propose a technique for the automatic extraction of cross-sections, the identification of water surface elevation, bluff heights and the possibility of distinguishing the signature of natural versus artificial features. Chapter 6 presents a new non-local sediment flux formulation for modeling fluvial erosion and compares the statistical features of the modeled landscapes to those of real ones. Lastly in Chapter 7, we summarize our research and elaborate on the prospects for future research in this area.

Chapter 2

Background

In this chapter, brief overviews are provided of (1) multi-scale filtering via wavelets, (2) nonlinear filtering, (3) geodesics and energy minimization principles, and (4) the wavelet-based geomorphic feature extraction methodology proposed by Lashermes et al. [26].

2.1 Wavelet linear filtering of digital elevation data

Let us call $h_0(x, y)$ the original high resolution elevation data given. Typically a *smoothing* filter is applied on the original data $h_0(x, y)$ to remove 'noise' (observational noise or irregularities at scales smaller than the scales of interest) and identify features as entities that persist over a range of scales. This operation of smoothing is also very important to make computations such as derivatives mathematically well-posed.

A popular smoothing filter is the Gaussian kernel, which, when applied to $h_0(x, y)$, results in images, or landscapes in our applications, at coarser resolutions, i.e.,

$$h(x, y, t) = h_0(x, y) \star G(x, y; t) \tag{2.1}$$

where $\star$ denotes the convolution operation and $G(x, y; t)$ is a Gaussian kernel of standard deviation t (larger values of t result in coarser resolution landscapes), centered at location (x, y):

$$G_{x,y,t}(u, v) = \frac{1}{2\pi t} exp\left[-\frac{(u-x)^2 + (v-y)^2}{2t}\right] \tag{2.2}$$

The family of coarsened landscapes resulting from (2.1) may be seen as solutions of the linear heat or diffusion equation, e.g., see Koenderink [38], with the initial condition $h(x, y; 0) = h_0(x, y)$, i.e.,

$$\partial_t h(x, y, t) = \nabla \cdot (c \nabla h) = c \nabla^2 h \tag{2.3}$$

where c is the diffusion coefficient and ∇ is the gradient operator. Thus, processing the landscape with Gaussian filters of increasing spatial scale is equivalent to applying an isotropic diffusion equation over time on the landscape with the spatial scale of the filter (variance) and the time of diffusion being related to each other. Once the time of diffusion is fixed, the spatial scale over which the Gaussian smoothing is applied on the original landscape is spatially uniform, i.e., the landscape is uniformly diffused at all points and in all directions.

The choice of the Gaussian kernel as smoothing filter is motivated in part by two criteria defined by Koenderink [38] as (1) *causality* and (2) *homogeneity/isotropy*. The *causality* guarantees that no spurious feature should be generated at coarser resolutions, since any feature at a coarse level of resolution must have a cause at a finer level of resolution. This guarantees noise reduction in the original data as the resolution is coarsened. The *homogeneity/isotropy* criterion requires the blurring to be space invariant. The Gaussian kernel thus satisfies the standard 'scale-space paradigm' as stated by Koenderink [38]. It is noted, however, that the Gaussian filtering is isotropic and does not respect the natural boundaries of the features; rather it diffuses at the same rate throughout the landscape including across boundaries. This obviously degrades the spatial localization of these boundaries, especially at larger scales of smoothing. These boundaries represent, in the case of landscapes, important discontinuities such as crests and valleys and it is important that their location is accurately preserved in any multi-scale (or space-scale) filtering methodology.

2.2 Perona-Malik nonlinear filtering of digital elevation data

Perona and Malik [1] reformulated the above space-scale paradigm to address this issue. The new paradigm was reformulated to satisfy three criteria: (1) *causality*, as previously

stated by Koenderink [38], (2) *immediate localization*, which searches, at each resolution, for sharp and meaningful region boundaries, and (3) *piecewise smoothing*, which indicates preferential smoothing (intraregion rather than interregion).

In the standard linear diffusion equation (2.3), the diffusion coefficient c is constant, that is, independent of the space location. An extension to the Gaussian filtering is obtained by choosing the diffusion coefficient c to be a suitable function of spatial location, such that the new space-scale paradigm criteria are satisfied. The modified diffusion equation can be written as

$$\partial_t h(x, y, t) = \nabla \cdot [c(x, y, t) \nabla h] \tag{2.4}$$

where ∇ indicates as before the gradient operator. Note that (2.4) reduces to the linear diffusion equation (2.3) if $c(x, y, t)$ is constant.

If the location of a channel were known, then, in order to achieve noise reduction and edge preservation, smoothing should preferentially happen in the region outside and within the channel, rather than across its boundary. This could be achieved by setting $c = 0$ at the channel boundaries and $c = 1$ everywhere else. However the channel location is not known in advance, and what can be computed instead is an estimate of it, or some geometric characteristic that defines it, thereby stopping, or at least reducing, diffusion across the channel boundary.

Let $\vec{E}(x, y, t)$ denote the vector-valued function representing an estimate of the channel's location. The diffusion coefficient can be chosen as a function of the magnitude of $\vec{E}(x, y, t)$, i.e.,

$$c = p(\mid \vec{E} \mid) \tag{2.5}$$

where $p(\cdot)$ has to be designed such that it ideally does not allow diffusion across boundaries. Perona and Malik [1] have proposed a simple first estimate of the channel's location (or image edges in their original application), given by the gradient of the elevation $h(x, y; t)$ at the location (x, y) and time t, i.e.,

$$\vec{E}(x, y, t) = \nabla h(x, y, t) \tag{2.6}$$

This provides a local estimator of the edges/discontinuities within the nonlinear space-scale paradigm. Note that we could also use curvature, area in combination with slope, or other higher order features to localize channels and thus define the diffusion coefficient

c, while the use of gradients is the most standard formulation in image processing and found to be sufficient for our application (see also discussion in Perona and Malik [1] for advantages of such a simple formulation). The diffusion equation thus takes the following form:

$$\partial_t h(x, y, t) = \nabla \cdot [p(\mid \nabla h \mid)\nabla h] \tag{2.7}$$

Perona and Malik suggested the following as possible edge-stopping functions:

$$p(\mid \nabla h \mid) = \frac{1}{1 + (\mid \nabla h \mid /\lambda)^2} \tag{2.8}$$

or

$$p(\mid \nabla h \mid) = e^{-(|\nabla h|/\lambda)^2} \tag{2.9}$$

where λ is a constant. Such expressions (when properly regularized, e.g., via an additional Gaussian smoothing, e.g., see [39]) of the edge-stopping function guarantee basic properties of the scale-space paradigm, while at the same time enhancing the discontinuities, thereby allowing their easier extraction (see [40, 1] and the following section for details). From a numerical point of view, we employ the version of the Perona-Malik filter proposed by Catté et al. [39]. The diffusion coefficient c is computed in the four directions (North, South, East, West) with the gradients in (2.8) or (2.9) computed through standard finite differences on Gaussian filtered data (with a very small standard deviation of the kernel $\sigma = 0.05m$), to avoid the stability issues related to the Perona-Malik original formulation [39]. Then, the gradients in (2.7) are computed on the non-smoothed data through standard finite differences, multiplied by the diffusion coefficient in each direction and then summed to advance in time.

We have constructed an example to show the effect of Gaussian (linear) versus Perona-Malik (nonlinear) filtering on an idealized landscape (Fig. 2.1(a)) with noise added on the surface. The white band represents an idealized ridge at a higher elevation compared to the surrounding landscape. As shown in Fig. 2.1(b) Gaussian filtering (standard deviation of the kernel $\sigma = 7m$ which corresponds to $t = \sigma^2 = 49$) achieves noise reduction at the expense of the localization of the ridge, as it appears diffused in the neighboring landscape. The Perona-Malik filter (Fig. 2.1(c) after $t = 50$ iterations) achieves noise reduction without affecting the boundaries localization. Note how after further processing the idealized landscape through Gaussian filtering (Fig. 2.1(d) with

$\sigma = 14m$ which corresponds to $t = 196$) the ridge and its location are not identifiable anymore, while the Perona-Malik filtering (Fig. 2.1(e) with $t = 200$) only improves noise reduction, without affecting the feature. In addition, Fig. 2.2 shows the profiles extracted from the idealized landscape shown in Fig. 2.1. Fig. 2.2(a) shows the case of an idealized landscape with no noise added on the surface. Note how the profile extracted from the Perona-Malik filtered data after $t = 50$ iterations resembles the original one, while the idealized ridge has almost disappeared from the Gaussian filtered landscape. The profiles shown in Fig. 2.2(b) and (c) refer to the same idealized landscape with noise added on the surface shown in Fig. 2.1. Note how well defined and enhanced appears the ridge after further Perona-Malik filtering of the data. This is due to the fact that at the boundary between the ridge and the surrounding landscape the gradients are large, thus diffusion is stopped.

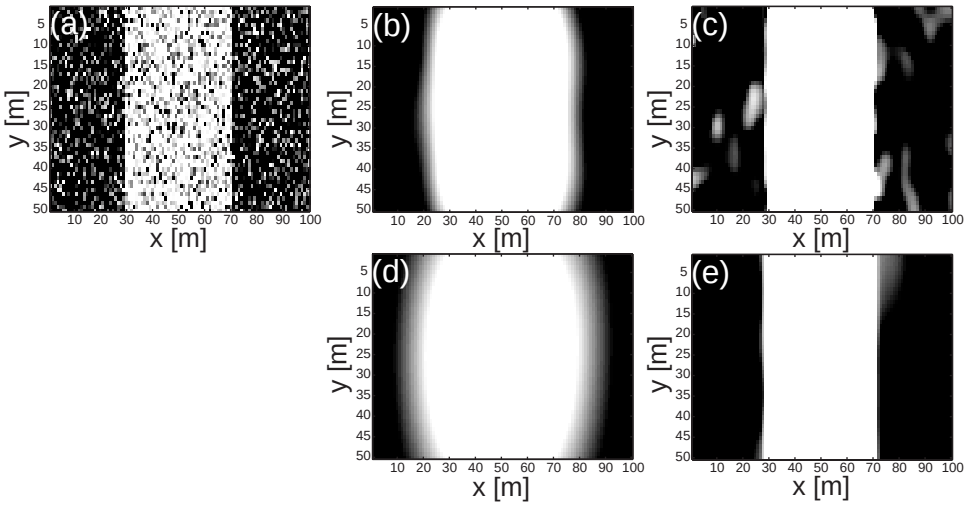

Figure 2.1: Comparison of the effect of Gaussian (linear) versus Perona-Malik (nonlinear) filtering on an idealized landscape. The white area represents an idealized ridge, with an elevation higher than the surrounding landscape. Noise has been added on the original data (a). Gaussian filtering achieves noise reduction at the expense of the boundaries localization (standard deviation of the kernel $\sigma = 7m$) (b), while Perona-Malik filtering achieves noise reduction, while preserving the right localization, avoiding diffusion across its boundaries (number of iterations $t = 50$) (c). Note how further processing with Gaussian filtering results in a completely blurred ridge ($\sigma = 14m$) (d), while the Perona-Malik filtering operation only reduces the noise further, without affecting the feature and its localization ($t = 200$) (e).

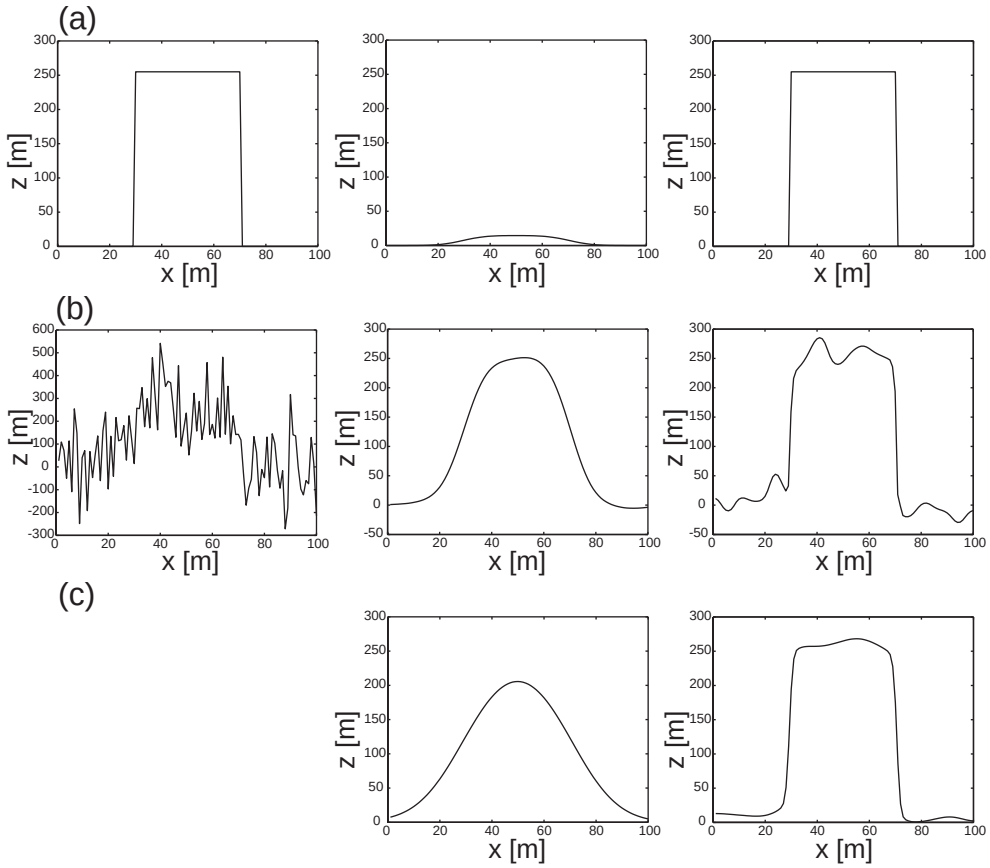

Figure 2.2: 1-d representation of the example shown in Fig. 2.1. (a) Idealized landscape with no noise added on the surface. Profiles extracted from the original idealized landscape (left), the Gaussian filtered landscape ($\sigma = 7m$) (middle) and the Perona-Malik filtered landscape ($t = 50$) (right). (b) Idealized landscape with noise added on the surface as shown in Fig. 2.1. Profiles extracted from the original idealized landscape (left), the Gaussian filtered landscape ($\sigma = 7m$) (middle) and the Perona-Malik filtered landscape ($t = 50$) (right). (c) Effect of further smoothing on the data shown in (b). Profiles extracted from the Gaussian filtered landscape ($\sigma = 14m$) (middle), and Perona-Malik filtered landscape ($t = 200$) (right).

2.2.1 Properties of the Perona-Malik filter

We illustrate here the properties of the Perona-Malik filtering which make it an effective filter for edge detection. Specifically, following the original formulation of Perona and Malik [1], we demonstrate that this filter acts as a backward diffusion in regions of high gradients such that it results in enhancing these edges for easy extraction. We illustrate this via a simple 1-d example of an *edge* modeled as a step function convolved with a Gaussian, assumed to be aligned with the y axis (see Fig. 2.3). The divergence operator in this case simplifies as follows:

$$\nabla \cdot [c(x, y, t)\nabla h] = \partial_x [c(x, y, t)\partial_x h] \tag{2.10}$$

Choose c to be a function of the gradient of h: $c(x, y, t) = p[\partial_x h(x, y, t)]$ and define the flux: $\phi(\partial_x h) \equiv c \cdot \partial_x h \equiv p(h_x) \cdot h_x$. Then, the 1-D version of the nonlinear diffusion equation (2.7) becomes:

$$\partial_t h = \partial_x \phi(h_x) = \phi'(h_x) \cdot h_{xx} \tag{2.11}$$

We are interested in the variation in time of the slope of the edge, which is given by $\partial_t(h_x)$. If $c(\cdot) > 0$ and the function h is smooth, the order of differentiation may be inverted:

$$\partial_t(h_x) = \partial_x(h_t) = \partial_x[\partial_x \phi(h_x)] = \phi'' \cdot h_{xx}^2 + \phi' \cdot h_{xxx} \tag{2.12}$$

Assuming the edge to be oriented such that $h_x > 0$, then, at the point of inflection, being the point with maximum slope, $h_{xx} = 0$, and $h_{xxx} << 0$. Then as can be seen from (2.12) if $\phi'(h_x) > 0$ the slope of the edge decreases with time, while if $\phi'(h_x) < 0$ the slope increases with time (the edge becomes sharper with time). Several possible choices of the function $\phi(\cdot)$ exist, one being the following (see Fig. 2.4):

$$\phi(h_x) = C/(1 + (h_x/\lambda)^{1+\alpha}) \tag{2.13}$$

with $\alpha > 0$. This means that there is a certain threshold value related to λ and α, below which $\phi(\cdot)$ is monotonically increasing, and beyond which $\phi(\cdot)$ is monotonically decreasing, achieving noise reduction and edge enhancement. In a neighborhood of the steepest region of an edge, $\phi'(h_x)$ is negative, which means that the nonlinear spatial filtering acts as backwards diffusion in time, thus achieving edge enhancement, while preserving the advantages of the stability given by the maximum principle satisfied by

this type of elliptic equation. For more details the reader is referred to the original publication of Perona and Malik [1].

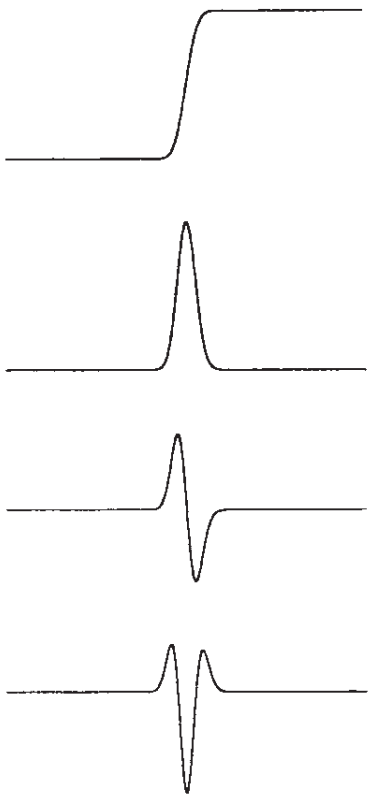

Figure 2.3: 1-d edge modeled as a step function convolved with a Gaussian kernel and its 1st, 2nd, and 3rd derivatives. Figure adapted from [1].

2.3 Geodesics and energy minimization principles for network extraction

If we have two fixed points a and b on the surface, we know there are infinite possible curves passing through them. If a and b now represent the outlet and a channel head of a tributary river network, then we know that among all the possible curves, only one will be a channel. Topographic attributes that distinguish channels from the rest of the landscape are the surface curvature and the flow accumulation. Channelized areas are,

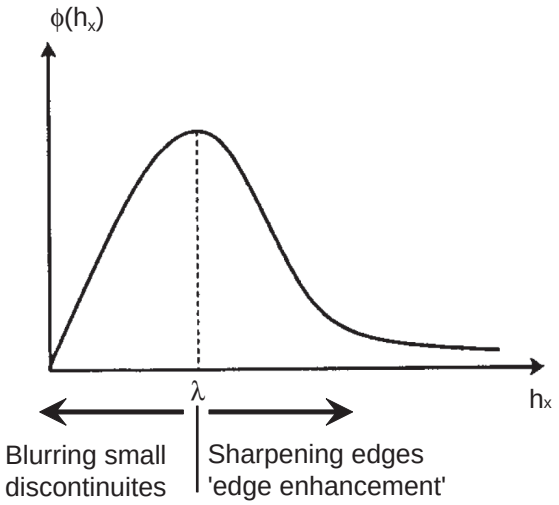

Figure 2.4: One form of the flux ϕ. There is a certain threshold value below which $\phi(\cdot)$ is monotonically increasing and beyond which $\phi(\cdot)$ is monotonically decreasing, achieving noise reduction and edge enhancement. Figure adapted from [1].

in fact, commonly characterized by positive curvature (or curvature above a threshold value which indicates convergent topography, while negative curvature indicates divergent topography correspondent to hillslopes) and by large values of flow accumulation (as channelized paths collect water in the downstream direction). If we were able to choose among all the possible curves connecting point a and point b (the outlet and a channel head of our river network) the one with the largest overall positive curvature and flow accumulation, then we would have identified the channel. This concept can be mathematically expressed through a function, called the 'cost function' and indicated by ψ, which represents the cost of traveling between point a and point b, in this case in terms of surface curvature and flow accumulation. This means that while the channel itself will be the curve with minimum cost (as will meet the requirements of positive curvature and large flow accumulation), the other curves will be penalized with a higher cost. The curve with the minimal cost corresponds to a mathematically defined quantity called the *geodesic curve* and formally defined as follows:

$$g(a,b) := \arg\left(\min_{C\in\Omega}\int_a^b \psi(s)ds\right) \tag{2.14}$$

where s is the standard Euclidean arc-length [41]. The minimum is taken over all the possible curves C that start at a and end at b.

Before we give more details on how the computation of the geodesic curve is performed, let us make two important observations related to the just introduced concepts. First, having said that for the detection of channels we define the cost function in terms of positive surface curvature and large flow accumulation, implies that different feature selections of the cost function will lead to different curves on the surface. This means that this approach could be used for the detection of other features of interest, such as roads or landslides for example, with the only challenge of being able to identify the most appropriate topographic attributes needed. Also, as it can be seen from equation (2.14), the integral sign indicates that the minimum is achieved in a global sense, not locally. If, for example, channels were to be traced following steepest descent directions, then the presence of noise in a pixel would deviate the channel in an erroneous way, while the global approach guarantees robustness. The same happens in the case of missing data: while forward marching techniques would stop, global approaches such as the geodesic framework would naturally "jump" over them, as they always connect the selected extreme points.

The computation of the geodesic curve involves another well defined mathematical quantity called *geodesic distance*:

$$d(a,x) := \min_{C\in\Omega} \int_a^x \psi(s)ds \tag{2.15}$$

This is the quantity which gives us the minimum distance from any point x to location a, computed by minimizing the cost function. Intuitively, we can now see how, if we want to travel from point a to point b along the geodesic curve (which in our case it means that we want to identify the channel that connects the outlet and a channel head), we need to use the information given by the geodesic distances. Formally, the actual geodesic curve is computed by gradient descent on the distance function $d(a,\cdot)$, backtracking from the 'downstream' point b. The geodesic is thus the integral curve of ∇d starting at b, and the gradient is intrinsically computed on the surface. Clearly, the efficiency of the computation of the geodesic curves depends on the computation of the geodesic distances. Several algorithms are available in the literature for the efficient computation of the geodesic distances [42, 43, 44, e.g.,]. These algorithms are applicable to all diverse

types of surface representations, from triangulated surfaces [45] to point cloud data as in LiDAR [46]. These extensions are based on the fact that the geodesic distance function satisfies a Hamilton-Jacobi geometric partial differential equation, $\mid \nabla d \mid = \psi$, where the gradient is intrinsic to the surface in the most general case. Additional information on these efficient computations can be found in [47, 48, 49, 50, 51]. Note that these algorithms are of linear complexity on the number of grid points, and thereby computationally optimal.

2.4 Review of a wavelet-based framework for feature extraction

Local slopes, $\mid \nabla h \mid$, and local curvatures, $\nabla^2 h$, carry considerable information about the type of landscape form at a site (e.g., valley, channel, hillslope, hollow). In particular, if a site i has $\nabla^2 h_i < 0$, the site is topographically convex, or divergent, and is conventionally defined as a hillslope. If $\nabla^2 h_i \geq 0$, the site is topographically concave, or convergent, and typically corresponds to a valley (channelized or not), hollow or basal hillslope sculpted by advective processes.

There are two different ways in which *scale* comes into the picture in the analysis of topographic data. First, there is the scale at which elevation data are available, usually called resolution. Second, there is a scale of averaging or smoothing that is often applied when computing local geomorphic properties. This smoothing, as said above, is performed to reduce the effect of noise or data inaccuracies on the numerical estimation of local derivatives from discrete data and also to focus the analysis on the scales of interest. This smoothing can be done traditionally in two different ways. One is to perform a spatial averaging of the pointwise derivatives, and the other is to spatially average the topography field and then take derivatives of the smoothed field. As shown by Lashermes et al. [26], smoothing the topography data with a Gaussian filter and then take first and second derivatives of the smoothed topography is mathematically equivalent to computing the wavelet coefficients of the topography using as wavelet filters the first and second derivatives of the Gaussian function, respectively. This is a direct consequence of the well-known property of the convolution product:

$$\partial_x (f \star g) = \partial_x f \star g = f \star \partial_x g \tag{2.16}$$

which implies that smoothing the function f with a kernel g and then taking derivatives (left most term) is equivalent to taking derivatives of the function and smoothing these derivatives with the kernel g (middle term) or equivalent to smoothing the function f directly with the derivative of the kernel g (right most term). This is an important property and its first two terms correspond to the smoothing methods just described. The third term of the above equality (2.16) naturally introduces the use of wavelets for efficient computation of local slopes and curvatures of a function. Specifically, the first and second derivatives of the function $h(x, y)$ in the x direction (similar expressions hold for the y direction) can be written as:

$$\nabla_{x,\sigma} h(x, y) = (h \star g^x_{1,\sigma,x,y})(x, y) \tag{2.17}$$

$$\nabla^2_{x,\sigma} h(x, y) = (h \star g^x_{2,\sigma,x,y})(x, y) \tag{2.18}$$

where:

$$g^x_{1,\sigma,x,y}(u, v) = \partial_x g_{0,\sigma,x,y} \tag{2.19}$$

$$g^x_{2,\sigma,x,y}(u, v) = \partial^2_x g_{0,\sigma,x,y} \tag{2.20}$$

and $g_{0,\sigma,x,y}$ is a 2D Gaussian kernel of standard deviation σ and centered at location (x, y), given by the expression for G in (2.2). We note that the above kernels (2.19) and (2.20) are proper wavelets, i.e., they satisfy the admissibility conditions of having local support and integral zero. By varying the variance σ of the Gaussian filter $g_{0,\sigma,x,y}$ (2.2) the above computations can be performed at different scales simultaneously.

The scale a associated with a wavelet $\psi(a, x)$ is defined from its Fourier transform $\tilde{\psi}(a, \nu)$: this has necessarily a well-defined maximum (a wavelet can be interpreted as a band-pass filter) at a specific frequency ν_m. The scale a is then defined as the inverse of this band-pass frequency: $a = \frac{1}{\nu_m}$ [52, 53]. Based on this, the scale a associated to the wavelets $g^x_{1,\sigma,x,y}$ and $g^y_{1,\sigma,x,y}$ is related to the parameter σ through the relation:

$$a = 2\pi\sigma \tag{2.21}$$

The scale a associated to the wavelets $g^x_{2,\sigma,x,y}$ and $g^y_{2,\sigma,x,y}$ is related to the parameter σ through the relation:

$$a = \sqrt{2}\pi\sigma \tag{2.22}$$

Since the scale a of smoothing is a more relevant and easier to interpret quantity than the parameter σ of the analyzing wavelet, all the notations for slope and curvature computed using wavelets will be labeled with a and not σ in the sequel. Note that a single choice for the scale a corresponds to different σ values for the g_1 and g_2 wavelets and thus for gradients and curvatures. The expression for the modulus $m_a(x, y)$ of the steepest slope at location (x, y) and scale a is given by:

$$m_a(x,y) = \sqrt{(\nabla_{x,a} h(x,y))^2 + (\nabla_{y,a} h(x,y))^2} \tag{2.23}$$

Channel incision in uplands topography leads to hillslopes on opposite sides that typically face each other obliquely. This signature can be used to delineate the axis of valleys and the likely pathway of channels with limited floodplain area on their boundaries [26]. This can be achieved by computing the derivative of the slope direction $\theta_a(x, y)$ given by:

$$d\theta_a = \sqrt{(d_x \theta_a)^2 + (d_y \theta_a)^2} \tag{2.24}$$

where:

$$\begin{aligned}
\theta_a(x,y) &= arctan\left(\frac{\nabla_{y,a} h(x,y)}{\nabla_{x,a} h(x,y)}\right) \text{ if } \nabla_{x,a} h(x,y) > 0 \\
&= \pi + arctan\left(\frac{\nabla_{y,a} h(x,y)}{\nabla_{x,a} h(x,y)}\right) \text{ if } \nabla_{x,a} h(x,y) < 0 \text{ and } \nabla_{y,a} h(x,y) > 0 \\
&= -\pi + arctan\left(\frac{\nabla_{y,a} h(x,y)}{\nabla_{x,a} h(x,y)}\right) \text{ if } \nabla_{x,a} h(x,y) < 0 \text{ and } \nabla_{y,a} h(x,y) < 0
\end{aligned} \tag{2.25}$$

and finding the points at which $d\theta_a$ becomes maximum (see Lashermes et al. [26]). Finally, the Laplacian is given by:

$$\gamma_a(x,y) = \nabla^2_{x,a} h(x,y) + \nabla^2_{y,a} h(x,y) \tag{2.26}$$

In Lashermes et al. [26] the above multiscale properties $\gamma_a(x, y)$ and $d\theta_a(x, y)$ were used to extract channel networks from LiDAR. Specifically, the analysis of the quantile-quantile plots of the Laplacian curvature and slope-direction-change across scales highlighted the existence of two transitions in the statistical behavior of these metrics [26]. It was found that a sharp deviation in the positive tails of the probability distribution of curvature from a Gaussian distribution defined a critical threshold curvature which

delineates the channelized valleys of the terrain, while the similarly identified threshold in the slope-direction-change indicates the transition between non-channelized and channelized parts of the valley. The two thresholds are used to create the set of the likely channelized pixels, namely a binary matrix called 'skeleton' where pixels that satisfy the threshold criteria are assigned a value of 1, while pixels that do not satisfy them are assigned a value of 0. The skeleton is then used as a starting point for a semi-automatic channel extraction algorithm.

Chapter 3

Geometric Framework for Channel Network Extraction from LiDAR

The objective of this chapter is to illustrate the concepts described in Chapter 2 through their application on LiDAR data of the South Fork Eel River basin in Northern California. We use the ALSM (Airborne Laser Swath Mapping) data (2.6 m average bare earth data spacing, gridded to 1 m) acquired by NCALM (National Center for Airborne Laser Mapping) (the data are available online at the data distribution archive http://www.ncalm.org/). We focus in particular on the Skunk Creek, a 0.54 km^2 landslide complex tributary located just upstream of the Elder Creek. The sub-basin and the location map are shown in Fig. 3.1. For the Skunk Creek we had available a hand-drawn channel network map (field survey done by Joel Scheingross and Eric Winchell, University of California, Berkeley). The digitized version of the hand-drawn map is shown in Fig. 3.1 as well. As can be seen, the part of the network close to the outlet is composed by *active* channels (channels with well defined banks and presence of bed material), while the part close to the divide consists of *inactive* (poorly formed channels with limited bed material but with definable channel banks) and *transient* channels (which present characteristics in between the inactive and active channels). Because the channel network of Skunk Creek is disrupted by deep-seated landsliding (see also

analysis of Gangodagamage et al. [31]) and is discontinuous in its upper reaches, several channel heads occur along individual valley paths (see Fig. 3.1). We preserve this discontinuity to explore how well we can detect not only channel initiation points but also channel disruptions through our proposed techniques. The channel network of the Skunk Creek is a very challenging basin for testing a channel extraction methodology. Nevertheless, the capability of our methodology in capturing channel disruptions, as shown in this section, makes it a very interesting application.

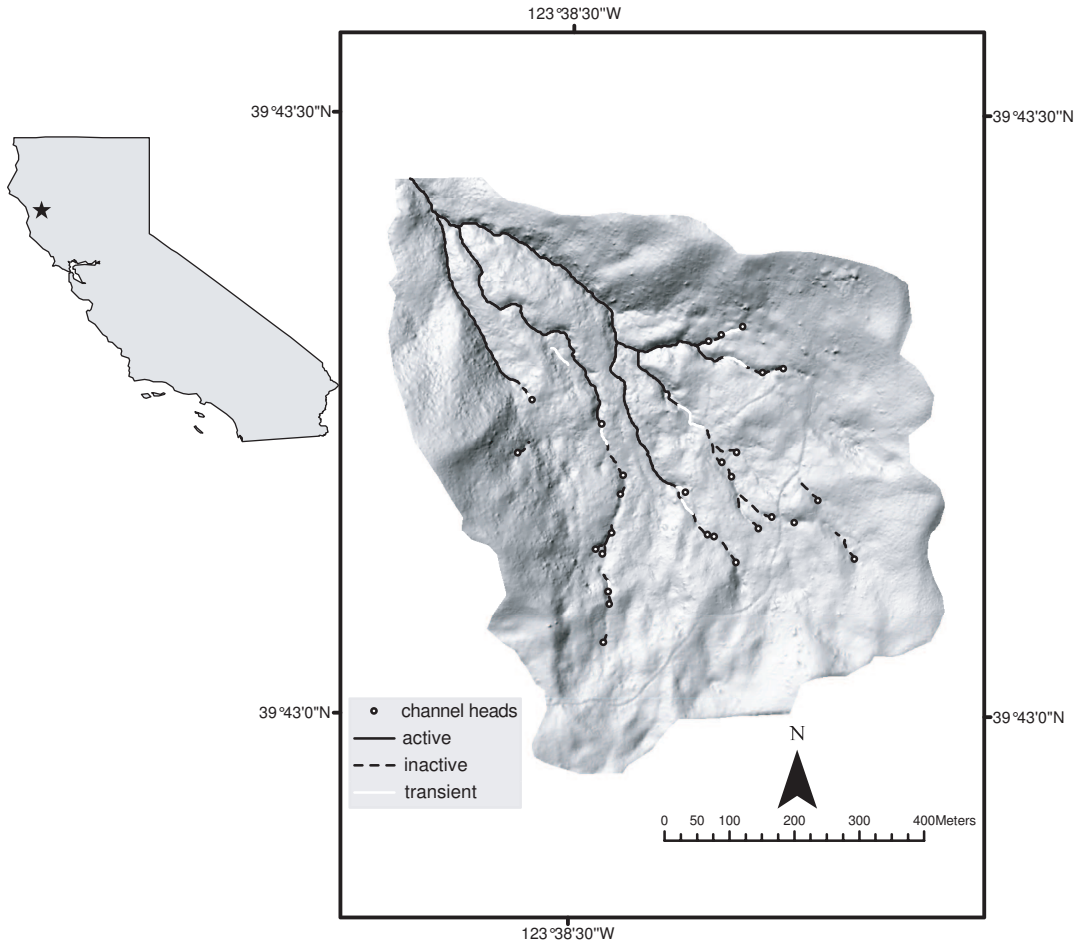

Figure 3.1: Skunk Creek, a 0.54 km^2 tributary located just upstream of Elder Creek, part of the South Fork Eel River in Northern California. The upper half of the basin consists of *active* channels (well defined banks and presence of bed material), while the bottom half consists of *inactive* (poorly formed channels with limited bed material) and *transient* channels (with characteristics in between active and inactive).

3.1 Pre-processing: Regularization of high resolution digital elevation data through nonlinear filtering

We focus our analysis on a 200m by 200m portion of the Skunk Creek, referred to as portion A (see Fig. 3.2). The landscape A has been processed with a Gaussian filter (isotropic linear diffusion) and the Perona-Malik filter (anisotropic nonlinear diffusion). To allow comparison of the two filtered landscapes, the time of forward diffusion (iteration steps) has been set to 50 iterations in both (in general, there is no exact mathematical correspondence between the corresponding diffusion times). This corresponds to a Gaussian spatial filter of approximate $\sigma = 7$m (scale of smoothing of the landscape of approximately $4\sigma = 28$m; see Table 1 of Lashermes et al. [26]). As is apparent from the theory, no such unique and uniform equivalent spatial scale of smoothing can be assigned to the nonlinearly filtered landscape as the effective smoothing scale varies locally at every point depending on the local gradient. Specifically, the effective spatial scale of smoothing is smaller in the vicinity of feature boundaries (e.g., the channel boundaries, where the gradient is large and the edge stopping function of equation (8) assigns a small diffusivity coefficient), and larger in areas of spatially homogeneous and small gradients (recall also the example shown in Fig. 2.1 and Fig. 2.2). The Perona-Malik filter used in this analysis is that of equation (8) with parameter λ estimated from the 90% quantile of the probability distribution function (PDF) of the gradients, as also suggested in Perona and Malik [1] (the selection of such a parameter can be made fully automatic also following the robust statistics approach in [54]). Note that the standard deviation of the Gaussian kernel and the number of iterations of the Perona-Malik filter have to be defined based on the scale of the objects we want to remove from the data. In particular the notion of 50 iterations has to be interpreted as a parameter of the algorithm. It represents the number of steps needed to achieve noise reduction and discontinuities enhancement before proceeding with the channel extraction.

Fig. 3.3(a) shows the original landscape at the resolution of 1m with 3m contours superimposed on it, as well as the computed gradients and curvatures (using simple first and second order numerical differentiation). Figs. 3.3(b) and 3.3(c) show the filtered landscapes with the Gaussian filter and Perona-Malik filter, respectively, using for both

50 iterations as the stopping time of the forward diffusion as explained above. The curvature reported here in all cases is the (geometric) curvature of the iso-height contours,

$$\kappa = \nabla \cdot (\nabla h / \mid \nabla h \mid) \tag{3.1}$$

computed by standard finite differences. The advantages in using the geometric curvature instead of the Laplacian will be addressed later in this chapter.

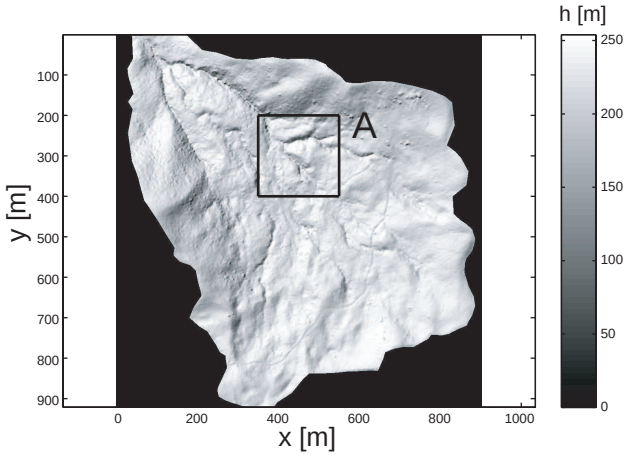

Figure 3.2: Location of the 200 m by 200 m square, named portion A, in Skunk Creek.

Several observations can be made from these figures. First, it is easily seen from Fig. 3.3(b) that the Gaussian filter smoothes the contours along the channels much more than the Perona-Malik filter. This is expected from the theoretical properties of the Perona-Malik filter which deforms the landscape much less along the discontinuities. In fact, the Perona-Malik filter achieves a limited deformation of contours along the discontinuities such that it encourages the localization of these features. It is also observed that the areas of the landscape over which the curvature is positive (along the channelized areas) are much broader, and thereby deformed, in the Gaussian filtered landscape than in the Perona-Malik landscape. This is also expected from the basic properties of the two filters. One can argue that the Gaussian filtering (isotropic diffusion) could be stopped earlier, i.e, smaller spatial scale of filtering, to result in better localization of the channelized valleys. However, as it will be seen later, such a smaller-scale filtering would not adequately eliminate the isolated high curvature areas that are not pertinent to channel extraction. Furthermore, nonlinear diffusion is enhancing the discontinuities

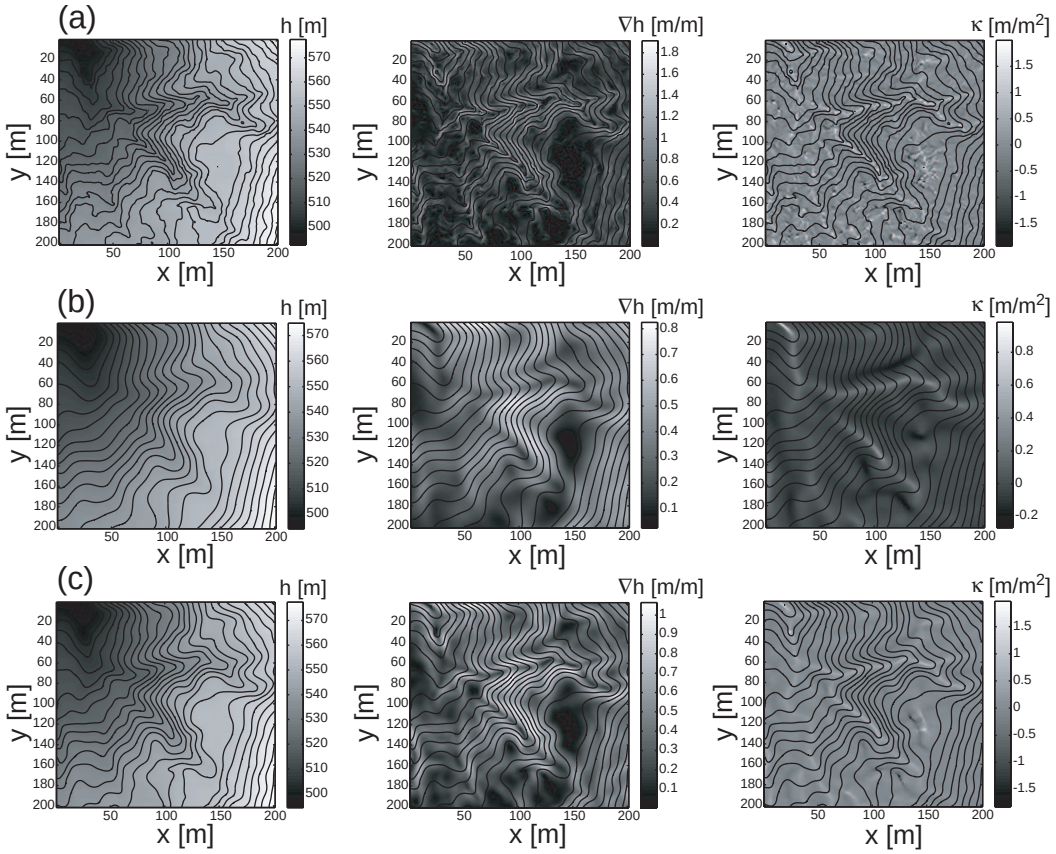

Figure 3.3: Comparison of elevation (left), gradient (middle) and curvature (right) between the original data (a), the Gaussian filtered data (scale $\sigma = 7$m) (b) and the Perona-Malik filtered data (50 iterations) (c), computed in portion A of Skunk Creek shown in Fig. 3.2. In all plots, elevation contours at 3m spacing are superimposed. Notice the sharper localization of the channels in the Perona-Malik filtered LiDAR data.

(acting in those regions as backward diffusion as shown in Perona and Malik [1]; see also Chapter 2), which is critical for facilitating the automatic channel network extraction.

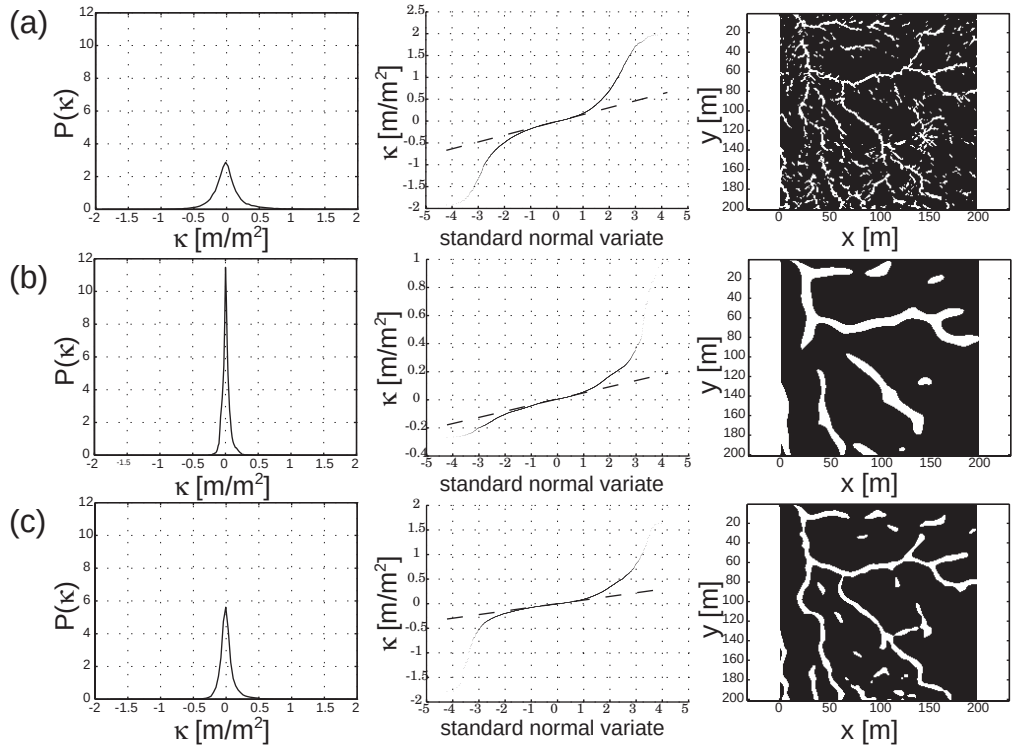

Figure 3.4: Comparison of the PDFs of curvature (left), q-q plots of curvature from which the threshold value is determined (middle), and skeleton of pixels with above-threshold-curvature for the original data (a), the Gaussian filtered data (scale $\sigma = 7$m) (b), and the Perona-Malik filtered data (50 iterations) (c), computed in portion A of Skunk Creek shown in Fig. 3.2. The Perona-Malik filter does the best in terms of accurately localizing the channelized valleys while reducing background noise (see text for more discussion).

Fig. 3.4 shows the PDFs of the geometric curvatures of the original data and the filtered landscapes as well as the quantile-quantile plots of those curvatures. As discussed in Lashermes et al. [26] for the Laplacian, the sudden change in the statistical signature of the landscape, depicted by the (positive) curvature at which the PDF deviates from a Gaussian PDF, marks the transition from hillslopes to valleys. It is interesting to observe that although the actual value of the threshold curvature is different for the original image and the two filtered images, as expected, the quantile at which this

transition occurs is scale- and filter-independent and as reported in Lashermes et al. [26] for the Laplacian, corresponds to the standard normal deviate of $z = 1$ (approximately the 84^{th} quantile of the PDF of curvatures). The right panels of Fig. 3.4 depict the pixels at which the curvature was greater than the threshold curvature identified from the corresponding PDFs; white pixels correspond to pixels with curvature greater than the threshold value while black pixels correspond to pixels with curvature smaller than the threshold value. Several observations can be made. First, the above-threshold-curvature pixels in the original high resolution data depict the channelized part of the landscape but at the same time one sees several isolated small areas which are strongly convergent due to the high frequency variability present on the landscape (e.g., bumpy ground, vegetation, etc.). The operation of smoothing is thus performed in order to focus the channel identification on the scale of interest. Second, the above-threshold-curvature pixels on the Gaussian filtered landscape eliminate the noise and nicely depict the valleys or channelized areas only; however, the corridors of the convergent areas are too wide due to the smoothing of the landscape which has been done at the scale of approximately 28m throughout the landscape.

The above-threshold-curvature pixels in the Perona-Malik filtered landscape (shown in Fig. 3.4(c)), depict in a much sharper way the channelized valleys. Of course, a smaller-scale Gaussian filter would also result in a sharper delineation of the channelized valleys. While this is true, however, the smaller scale of smoothing would not eliminate the isolated small convergent areas which are not part of the channel network. This is demonstrated in Fig. 3.5, which displays the above-threshold-curvature pixels for three standard deviations of the Gaussian filter: $\sigma = 2m$ (landscape smoothing scale $a = 8.9$m); $\sigma = 4$m (landscape smoothing scale $a = 17.8$m); $\sigma = 6$m (landscape smoothing scale $a = 26.7$m). It is noted by comparing Fig. 3.4(c) and Fig. 3.5, that the Perona-Malik localization of the channelized valleys (measured by the width of the white corridors) is comparable to the localization provided by the Gaussian filter at scale of approximately 9m ($\sigma = 2$m). However, at this small scale of smoothing, the Gaussian filtering results in many more isolated high curvature areas as can be seen in Fig. 3.5(a) compared to Fig. 3.4(c). Thus we conclude overall, that the Perona-Malik filter is a more efficient filter to use for pre-processing of the raw data (to produce what is called 'regularized data') on which further operations for automatic channel extraction can be

performed.

It is also worth pointing out the advantage of using the (geometric) curvature κ instead of the Laplacian. This can be seen by comparing Fig. 3.4(b) to Fig. 3.6. The figures show the skeletons of pixels above-threshold-curvature obtained on the Gaussian filtered data (scale $\sigma = 7$m) using geometric curvature (Fig. 3.4(b)) and Laplacian (Fig. 3.6). Note how sharper and well defined is the skeleton obtained using the geometric curvature.

Before demonstrating in the next section the geodesic energy minimization approach for the automatic extraction of the whole channel network of the Skunk Creek, we note that one can further process the regularized data to eliminate even more the occasional isolated convergent pixels seen in Fig. 3.4(c). This is a further operation which can be easily done via a contributing-area-threshold, where the threshold used has to be small enough not to interfere with channel initiation. For example, Fig. 3.7 shows the skeleton of Fig. 3.4(c) after applying the additional contributing area threshold of $A = 3000\ m^2$, meaning that only the pixels with contributing area equal to or above this threshold were selected. The contributing area was computed using the Dinf algorithm [55]. We have then compared this value to the minimum contributing area at the channel heads, obtained using the same algorithm at the 11 farthest surveyed channel heads in Skunk Creek. As it can be seen from the histogram of the contributing area shown in Fig. 3.8, the minimum value is equal to 3329 m^2, thus the chosen contributing area threshold of 3000 m^2 does not interfere with channel initiation. It is noted that, while the curvature threshold is easily identifiable from the quantile-quantile plot, as explained earlier, the contributing area threshold is an arbitrarily chosen value, the smallest able to reduce the noise further in the skeleton of likely channelized pixels. It is observed that this further operation not only removes isolated convergent areas, but also further narrows the width of the likely channelized valleys providing a better pre-processed data on which channel heads are identified for the geodesic optimization to be performed.

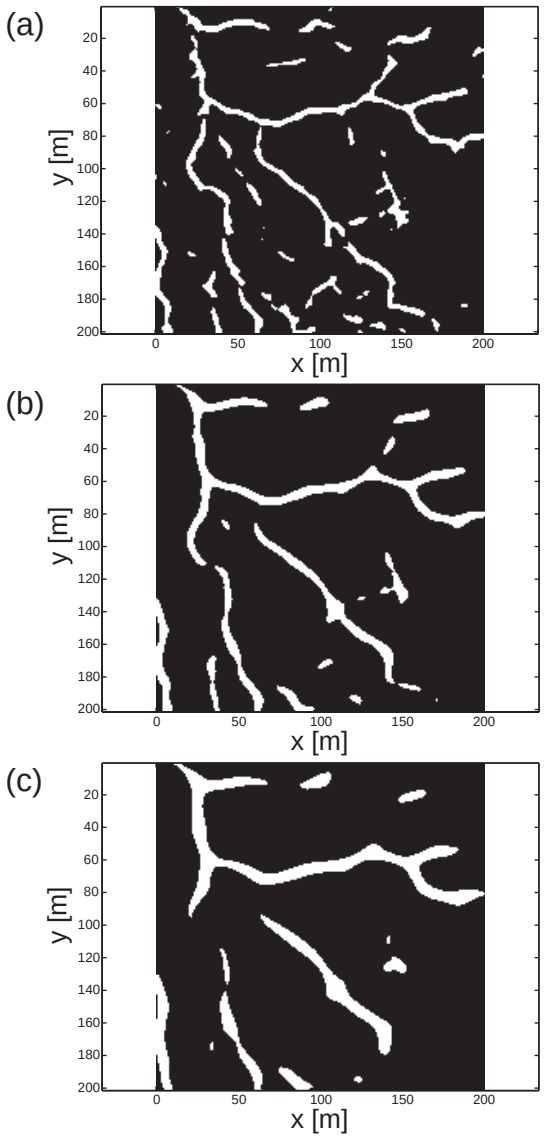

Figure 3.5: Comparison of the images obtained thresholding the curvature computed on the Gaussian filtered data with $\sigma = 2$ m,4 m,6 m (landscape smoothing scales of 8.9 m, 17.8 m, and 26.7 m) respectively. White pixels indicate pixels with above-threshold curvature. The plots refer to portion A of Skunk Creek shown in Fig. 3.2.

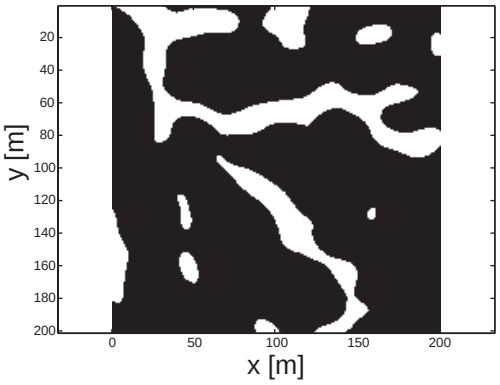

Figure 3.6: Skeleton of pixels above-threshold-curvature for the Gaussian filtered data using the Laplacian with $\sigma = 7$m (landscape smoothing scale of 31.1 m). The plot refers to portion A of Skunk Creek shown in Fig. 3.2.

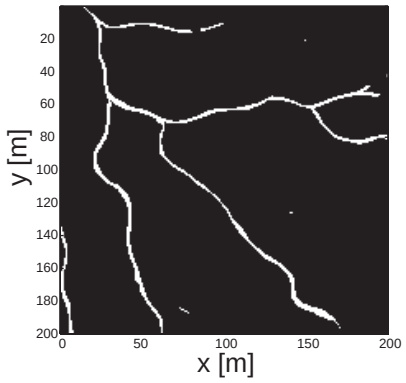

Figure 3.7: Skeleton obtained by thresholding curvature and contributing area for the portion A of Skunk Creek shown in Fig. 3.2. Introducing the contributing area criterion eliminates all the isolated pixels which have a positive curvature above threshold, but are not part of the channel network.

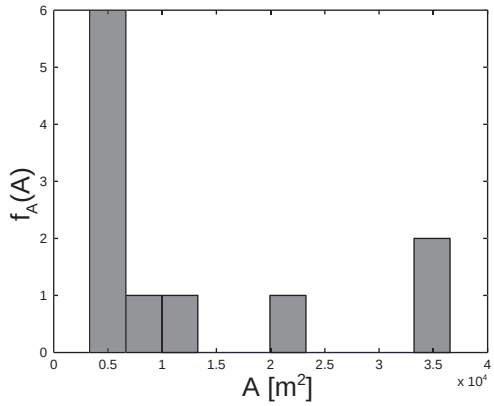

Figure 3.8: Histogram of the contributing area computed with the Dinf algorithm at the 11 farthest channel heads surveyed in Skunk Creek.

3.2 Automatic extraction of channel paths from the regularized data

In this section we focus on the regularized data set of Skunk Creek obtained through nonlinear filtering and illustrate how the concepts of geodesics and energy minimization described earlier allow a fast and efficient extraction of the channel network. The first step of the extraction procedure is the creation of the skeleton obtained by nonlinear filtering and thresholding the curvature and the contributing area, as discussed in the previous section. The threshold curvature was easily identified by a clear change in the statistical behavior of the curvature, while the threshold area was set to a value of 3000 m^2. The extracted skeleton for the Skunk Creek river basin is shown in Fig. 3.9.

Several observations can be made by comparing Fig. 3.9 with the surveyed network shown in Fig. 3.1. First, in Fig. 3.1 one observes that most of the channels in the part of the network close to the divide are labeled as 'transient' or 'inactive' and indeed the extracted skeleton depicts this topography by a series of interrupted areas of high curvature (and large contributing area). Second, at the points where the surveyed channel heads are located, our algorithm depicts a substantial interruption in the channelized valley. It is observed therefore, that the pre-processing already allows one to investigate more closely the richness of the landscape form, something not possible with other current algorithms.

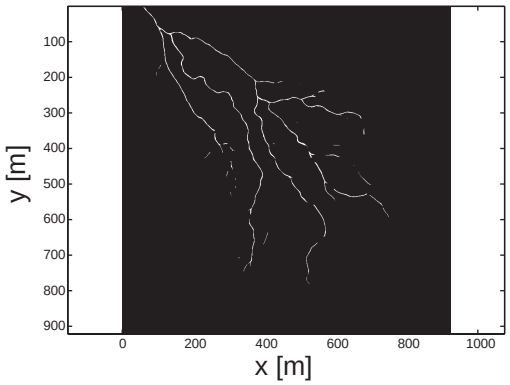

Figure 3.9: Skeleton obtained by thresholding curvature and contributing area for Skunk Creek.

From the skeleton of Fig. 3.9, we can detect the river network outlet, as the point with the maximum flow accumulation area, computed, for example, using the Dinf algorithm [55]. After the outlet of the network has been identified, we can proceed with the detection of the end points. First the algorithm uses the skeleton of Fig. 3.9 to compute how many continuous elements compose the skeleton and how many pixels belong to each of them. With this we mean that we label with a sequential number all the parts of the skeleton which are completely connected and do not present disruptions (i.e., the skeleton is continuously equal to 1, while the disruption is represented by one or more pixels equal to zero). We call the variable representing the number of pixels in each connected element N and plot in Fig. 3.10(a) its histogram. As it can be seen, the Skunk Creek skeleton is composed by 56 connected elements, one of which is composed by 4508 pixels and 55 much smaller elements. This is something we could have expected having already observed that Skunk Creek is an extremely disrupted basin, and we can deduce that the element composed by 4508 pixels is the one which includes the part of the basin close to the outlet (the most continuous one), while the 55 smallest elements compose the skeleton of the part of the basin close to the divide (which, as we already pointed out, appears extremely disrupted in agreement with the fact that the channels here are either inactive or transient). Note that some of these elements may also represent small isolated noisy areas still present in the data.

Now that the connected elements of the skeleton are identified, the algorithm looks for the end points. These are identified as the points at which the branches end. Since

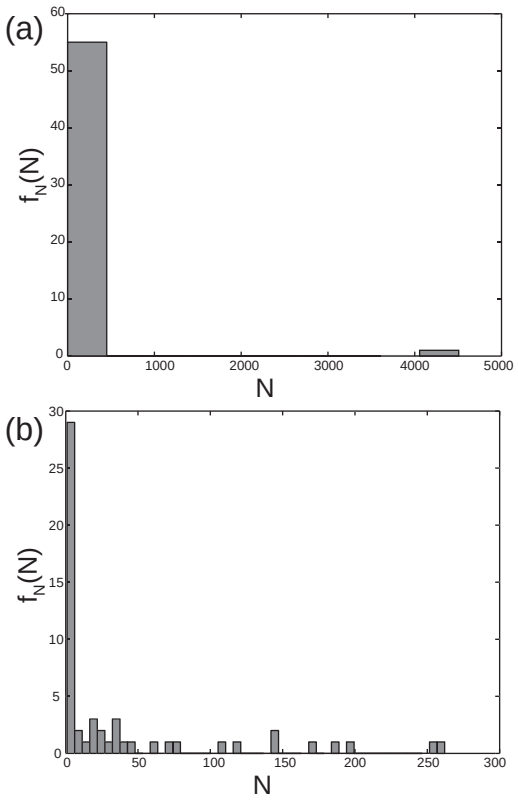

Figure 3.10: Histogram of the number of pixels belonging to each connected element of the skeleton of Skunk Creek. The skeleton is composed by 56 elements of which one includes the majority of the pixels (a). Excluding the most connected element, the histogram highlights a large number of small connected elements below and around $N = 10$ pixels. This value can be interpreted as the size of small isolated convergent areas which do not belong to channels (b).

the branches are wider than one pixel, the actual point taken as end point is the one which belongs to the minimum geodesic distance path. Thus we need to define the cost function which will be used to identify the end points and connect them to the outlet through geodesic curves. This *cost function* was chosen to give penalty for selecting paths along which the drainage area does not have large flow accumulation and along which the curvature is not large compared to the surrounding points. The chosen form of the cost function ψ used in (2.14) is the following:

$$\psi = \frac{1}{(\alpha \cdot A + \delta \cdot \kappa)} \tag{3.2}$$

where A is the contributing area, κ is the curvature (of iso-height contours for our examples), and α and δ are constants which have to be chosen appropriately for the application at hand. The purpose of these constants is to take care of the dimensionality of ψ (as A is measured in m^2, while κ in $1/m$) and of the difference in the order of magnitude between the quantities employed (A varies between 1 and $5 \cdot 10^5$ m^2, while κ has been normalized and thus varies between 0 and 1).

We will discuss later in this section how the choice of the constants α and δ can be made. For now, to illustrate how the end points are detected, let us assume we have identified the optimal parameters of the cost function (3.2) for our application, namely $\alpha = 1\ m^{-2}$ and $\delta = 10^3\ m$ (see discussion later in this section on how these parameters can be determined). We focus on the $200m$ by $200m$ portion A of the Skunk Creek used in Section 3.1. Fig. 3.11(a) shows the skeleton of Skunk Creek (the same previously shown in Fig. 3.7) and Fig. 3.11(b) shows the end points as detected by the algorithm and indicated by a white circle. We can notice that the locations marked as A, B and C do not appear to belong to a channel, but rather to be small convergent areas still present in the skeleton after pre-processing. It is clear that we need to identify these elements and ignore them, such that they will not be erroneously considered as channels. If we plot again the histogram of N, the number of pixels belonging to each connected element of the skeleton, ignoring the largest element, as shown in Fig. 3.10(b), we notice that there is a large number of small connected elements located below and around a value of $N = 10$ pixels. We can interpret these elements as small isolated convergent areas and detect the end points only on the elements of the skeleton with $N > 10$ pixels. Note that we expect the identification of this threshold of N to be much simpler

in the case of a basin more homogeneous than Skunk Creek. Due to the nature of the basin here in analysis, the choice of this value of N is extremely challenging, while a more homogeneous basin would probably present the skeleton as a unique connected element, with a few smaller ones, which could be easily interpreted as isolated areas. The result of adding a threshold $N > 10$ pixels in the end points detection can be seen in Fig. 3.11(c). Locations A, B and C are now ignored and the end points (indicated by white circles) are identified only on the branches that appear to be channels. Following this procedure we have identified all the end points in the Skunk Creek skeleton, as shown in Fig. 3.12.

After all the end points have been detected, we connect them with geodesic curves through the above defined cost function (3.2). Let us now discuss the selection of the constants α and δ. A helpful quantity in the definition of the constants α and δ is the geodesic distance d (2.15). Since the geodesic curves (2.14) are computed by gradient descent on d, then d can be used to understand how optimal is the choice of the constants. This is illustrated in Fig. 3.13. The figures labeled from (a) to (j) show the geodesic distances d and the extracted network correspondent to different choices of α and δ in the cost function ψ (3.2). Fig. 3.13(a) and Fig. 3.13(c) show the geodesic distances d corresponding to $\alpha = 1\ m^{-2}$ and $\delta = 0\ m$ and $\alpha = 0\ m^{-2}$ and $\delta = 1\ m$ respectively, and Fig. 3.13(b) and Fig. 3.13(d) the corresponding extracted networks. It is clear that using only one of the two quantities does not give good results. Figures 3.13 (e) through (j) show the geodesic distances and the extracted networks for $\alpha = 1\ m^{-2}$ and $\delta = 1,\ 10^3,\ 10^5\ m$. It can be seen how the choice of $\alpha = 1\ m^{-2}$ and $\delta = 1000\ m$ gives the smallest values of the geodesic distance along the skeleton of the network. This can be used as guidance to ensure an optimal computation of the geodesic curves. Note that the value of $\delta = 1000\ m$ corresponds to the order of magnitude of the mean contributing area computed on the whole surface $\bar{A} \simeq 550\ m^2$.

Fig. 3.14 shows the extracted channel network obtained for the Skunk Creek with $\alpha = 1\ m^{-2}$ and $\delta = 1000\ m$ and compared to the surveyed data. As discussed before, this is a challenging basin for the automatic channel network extraction due to many interruptions due to landslides and debris flows. Nevertheless, the automatically extracted channel network compares well with the field-surveyed river network. Recall that the only information that was externally provided was the threshold area of

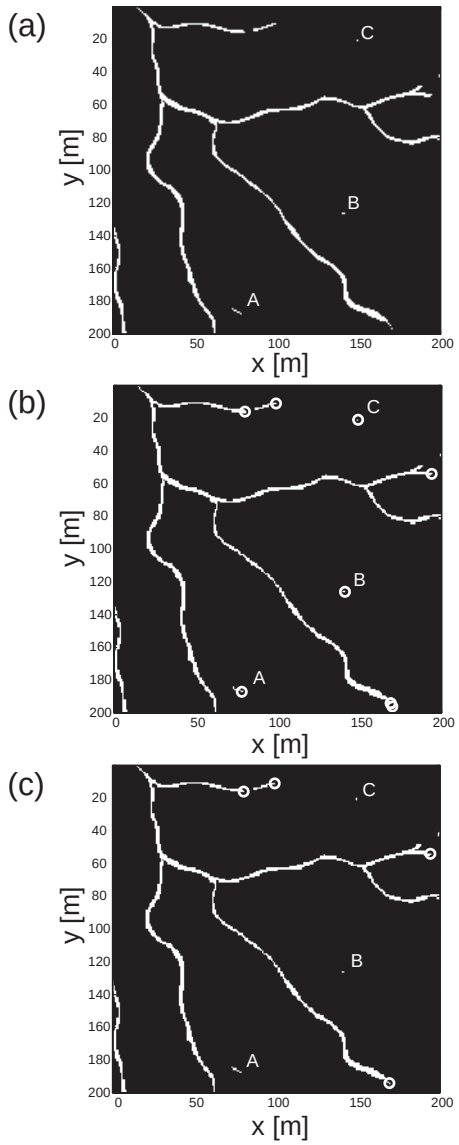

Figure 3.11: Detection of the end points. Skeleton obtained thresholding curvature and contributing area in portion A of Skunk Creek (a). Without a threshold in N, the number of pixels composing each connected element, locations A and B are identified as channels (b). The threshold $N > 10$ pixels allows to exclude locations A and B from the end points detection (c). End points are here indicated by a white circle.

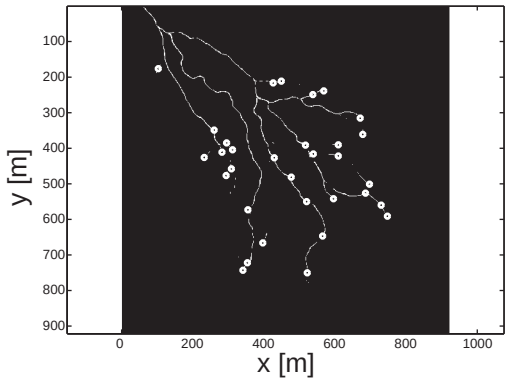

Figure 3.12: End points automatically detected in Skunk Creek.

3000 m^2 and the values of the parameters α and δ, though guidelines for the possible automatic selection of these parameters were provided as well.

As discussed earlier, our algorithm allows the detection of channel disruptions (see Fig. 3.9) which are depicted in the skeleton and can be kept before the geodesic optimization is performed. The channels are traced continuously to the farthest end points detected, but the user knows the location and the extent of the disruptions from the skeleton. Figs. 3.15(a) and 3.15(b) show the histogram of the length of the channel disruptions measured on the surveyed data of Fig. 3.1 and on the extracted skeleton of Fig. 3.9. As it can be seen the extracted network of Skunk Creek shows, statistically, the same level of disruptiveness characteristic of the area.

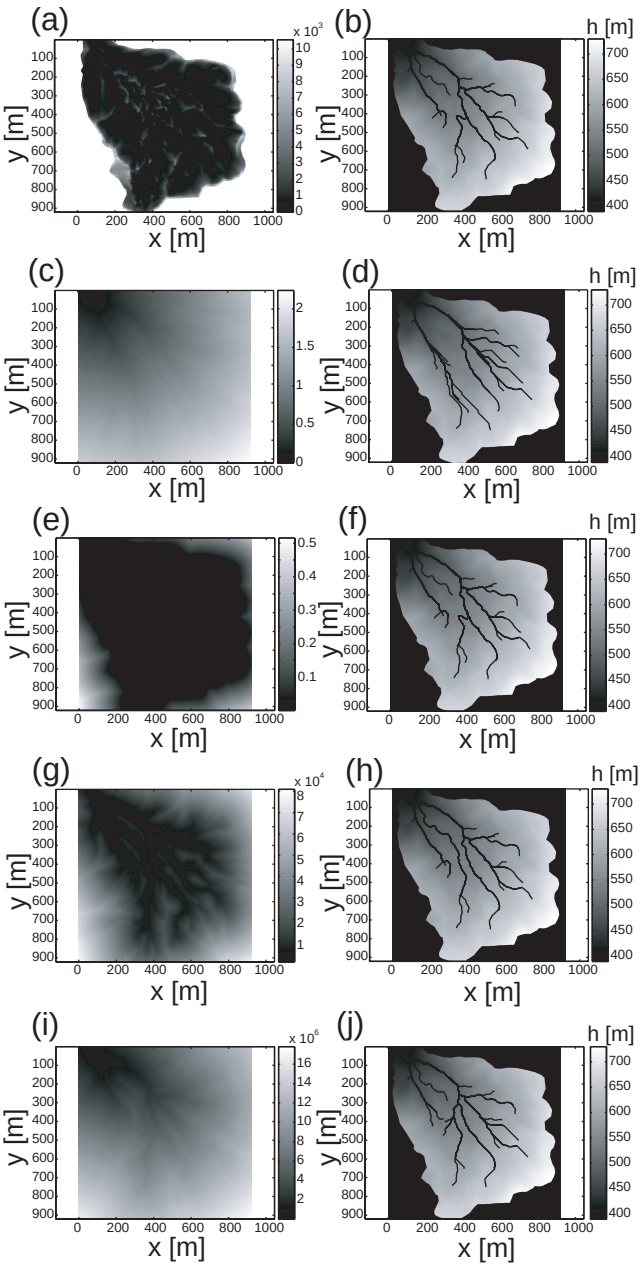

Figure 3.13: The geodesic distances d and the extracted networks for different choices of the parameters of the cost function ψ. The geodesic distances are useful in understanding if the choice of the cost function guarantees the optimal tracing of geodesic curves. (a) and (b) $\psi = \frac{1}{A}$; (c) and (d) $\psi = \frac{1}{\kappa}$; (e) and (f) $\psi = \frac{1}{A+\kappa}$; (g) and (h) $\psi = \frac{1}{A+10^3 \cdot \kappa}$; (i) and (j) $\psi = \frac{1}{A+10^5 \cdot \kappa}$.

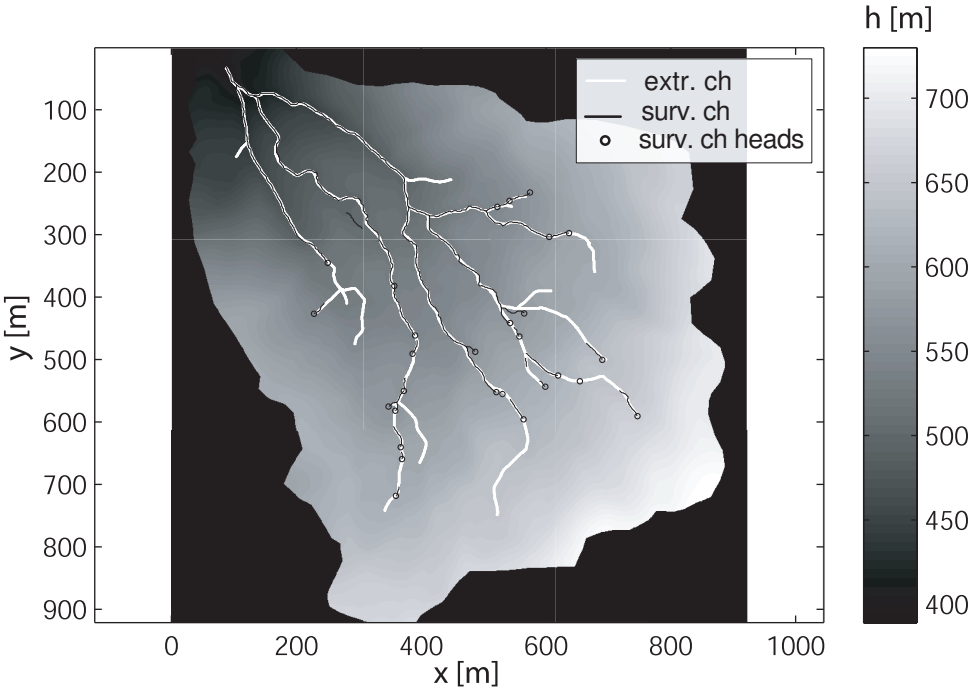

Figure 3.14: Automatically extracted river network for Skunk Creek using the geodesic optimization on the Perona-Malik filtered landscape, compared to the digitized surveyed data.

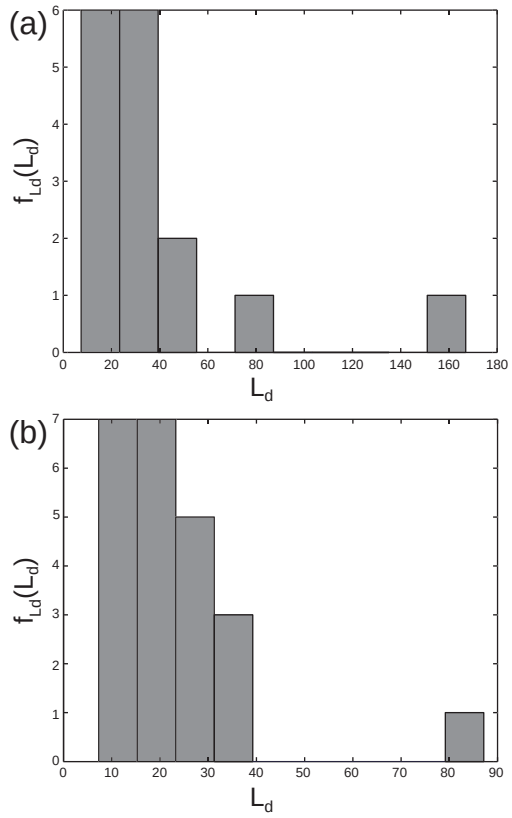

Figure 3.15: Histogram of the length of the channel disruptions L_d measured on the surveyed data (a). Histogram of the length of the channel disruptions L_d measured on the extracted data (b).

Chapter 4

Space-scale Methodologies in a Complex Mountainous Landscape

The aim of this chapter it to test and compare the relative merits of the methodologies proposed by Lashermes et al. [26] and Passalacqua et al. [56] (reported in Chapter 3) in terms of their capability of extracting geomorphic features of interest such as channel heads, detecting relevant channel disruptions corresponding to landslides, and capturing representative channel cross-sections. The study area is part of the Rio Cordon basin, a headwater alpine catchment located in the Dolomites, a mountainous region in the Eastern Italian Alps. The basin is morphologically divided into two parts: the upper part consists of a low-slope belt dominated by colluvial channels; the lower part displays steep slopes and a narrow valley where alluvial channels are dominant and shallow landslides are present. We selected this test area because several field surveys were conducted during the past few years, including LiDAR (Light Detection and Ranging), field mapped channels, channel heads and landslide scars. We take advantage of the survey data available, to focus on the ability of the methodologies to localize channel heads. As pointed out in Lashermes et al. [26] and Passalacqua et al. [56], the methodologies produce 'skeletons' of likely channelized pixels which are discontinuous, meaning that the probable channels exhibit disruptions, which may or may not represent geomorphologic features of interest. We investigate the nature of these disruptions by taking advantage

of the availability of survey-mapped landslides. Furthermore, the effect of linear versus nonlinear filtering is analyzed through the investigation of cross-sections extracted along the channels of Rio Col Duro. Finally, we suggest a guideline for such applications, and also identify future challenges in fully or almost fully automated methodologies for geomorphic feature extraction from LiDAR.

4.1 Study area

The study area (Fig. 4.1) consists in the Rio Col Duro basin (subbasin of Rio Cordon), a small head water basin of 0.45 km^2, and some neighboring landslide areas, located in the Dolomites, a mountainous region in the Eastern Italian Alps. The elevation ranges from 1935 to 2385 m a.s.l. with an average of 2199 m. The slope angle is 25° on the average and 74° at maximum, computed at the catchment relief scale. The basin is morphologically divided into two parts: the upper part consists of a low-slope belt dominated by colluvial channels; the lower part displays steep slopes and a narrow valley, where bedrock and alluvial channels and shallow landslides are present.

The area has a typical alpine climate with a mean annual rainfall of about 1100 mm. Precipitation occurs mainly as snowfall from November to April. Runoff is dominated by snowmelt in May and June, but summer and early autumn floods represent an important contribution to the flow regime. During summer, storm events are usually separated by long dry spells. Soil thickness varies between 0.2 and 0.5 m on topographic spurs to depths of up to 1.5 m on topographic hollows. The vegetation covers 98% of the basin and consists of high altitude grassland (92% of the area, of which about 16% are vegetated talus deposits), and sporadic tall forest (6%). The remaining 2% of the area consists of bedrock outcrops and unvegetated talus deposits. Several field surveys were conducted during the past few years including LiDAR surveys (data acquired during snow free conditions in October 2006). A recent campaign (September-October 2008, and August 2009) has provided new detailed data of field-mapped alluvial and colluvial channels, channel heads, and landslide scars in a neighboring area.

The shallow landslides related to the study area were documented by repeated surveys in the period 1995-2001, and summer 2008-2009 based on DGPS (Differential Global Positioning System) ground observations. Analysis of these data indicates that

small, shallow debris flow scars heal rapidly, and are difficult to detect after as few as 3-4 years. About 68% of the surveyed landslides were triggered by a very intense and short-duration storm on September 14, 1994 [57, 58]. The storm, with a duration of 6 hr, caused the largest flood recorded in 20 years of observation in the Rio Cordon basin. Due to the short duration of the storm, few slope instabilities were observed on entirely soil-covered slopes, while several landslides were triggered on slopes just below rocky outcrops [59]. An important new sediment source was formed on May 11, 2001, during an intense snowmelt event without rainfall following a very snowy winter [58]. Soil saturation mobilized a shallow landslide covering an area of 1905 m^2 which then turned into a mud flow moving along a small tributary. This new landslide area triggered during 2001 is considered in this work, and it is located in a neighboring area of the Rio Col Duro basin where steep slopes, a narrow valley, and ancient landslide deposits are present. The location map of Rio Col Duro and the available surveyed data (channels, channel heads and landslides) are shown in Fig. 4.1.

4.1.1 Field data collection

Field surveys were carried out along the entire hydrographic network. The catchment was systematically walked along all the drainage lines up to the catchment divide. The channel head, or first-order stream head, was defined as the point at which non-confined divergent flows on the hillslope converged to a drainage line with a well-defined flow path, i.e., the upstream limit of concentrated flow [60].

The channel network identified in the Rio Col Duro basin can be divided into three portions: colluvial, bedrock, and alluvial channels (see Fig. 4.1). The colluvial incisions are small headwater channels, exhibiting a weak or ephemeral transport capacity [61]. They can be considered as the elementary component of the hydrologic network, defining channel initiation [62], and characterizing the headwater areas. In our study area these formations are dominant in the upper part of the basin, where gentle slope prevails. The initiation process is due to an upslope infiltration of water within moraine deposits, and downslope subsurface flow where gentle slope soil mantle prevails. Nevertheless, colluvial channels are also present in the lower and steeper part of the basin, where their formation is mainly due to flow accumulation and surface erosion due to larger values of slope. The alluvial channel network (low-mid zone of the network) is dominated

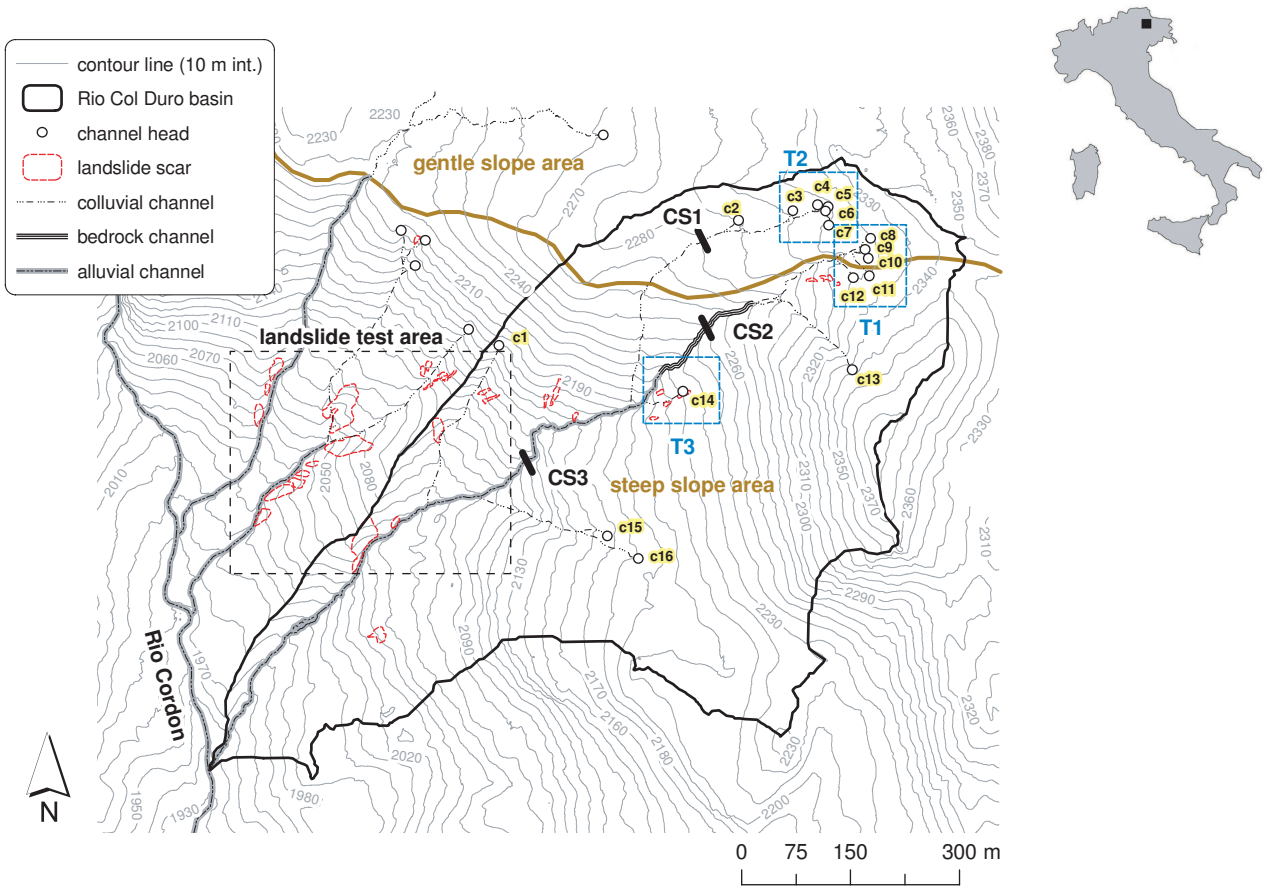

Figure 4.1: The Rio Col Duro basin. The figure shows the location map of the study area, the channel head locations *c*, the areas where the analysis of channel heads detection is performed (*T1*, *T2* and *T3*) and the area where landslide disruptions are analyzed (*landslide test area*). The locations of three extracted cross-sections are also marked (*CS1*, *CS2*, and *CS3*).

by erosional and depositional processes controlled mainly by local slope changes, where the sediment forming the channel bed can be transported and organized during floods. Alluvial channels are characterized by bed morphologies such as cascades and steep pools, typical of steep mountainous channel reaches, characterized by high transport capacity [63].

4.1.2 LiDAR data specifications

The LiDAR data and high resolution aerial photographs were acquired from an helicopter using an ALTM 3100 OPTECH, and Rollei H20 digital camera flying at an average altitude of 1000 m above ground level during snow-free conditions in October 2006. The flying speed was 80 knots, the scan angle 20° and the pulse rate 71 kHz. The survey design point density was specified to be greater than 5 points/m^2, recording up to 4 returns, including first and last. LiDAR point measurements were filtered into returns from vegetation and bare ground using the Terrascan^{TM} software classification routines and algorithms. The filtered point density was approximately 3 point/m^2. The LiDAR bare ground dataset was used to generate a Digital Terrain Model (DTM) of 1 m grid cell size. The vertical accuracy, evaluated by a direct comparison between LiDAR and ground DGPS elevation points, was estimated of less than 0.3 m, an acceptable value for many LiDAR analysis in the field of geomorphology [27, 28, 34, 64]. Digital aerial photos at a resolution of 0.15 m were also collected using a Rollei H20 camera.

4.2 Channel heads detection

The methodologies described in the previous section produce a skeleton of likely channelized pixels, meaning that among all the pixels belonging to the landscape, only the ones that satisfy the threshold criteria, are assigned a value equal to 1, while the pixels which do not satisfy one or both criteria are labeled as zero. The skeleton of likely channelized pixels gives us an idea of the channel network that will be extracted, of the extension of the channels and of possible significative channel disruptions. By comparing the extent of the probable channels with the surveyed locations of the channel heads, we can test whether the filtering and the threshold criteria chosen are able to detect channel initiation properly.

It is important to note that the Rio Col Duro basin exhibits a significant variability in the values of drainage area at the channel heads. Namely, among the 16 channel heads included in the basin, the channel initiation drainage area ranges between 110 m^2 and 5200 m^2 approximately, as it can be seen from the histogram of drainage areas in Fig. 4.2, computed using the Dinf algorithm [55]. It is clear that it would be difficult to capture such a variability with a unique threshold value for drainage area, as it would be required by a classic global extraction methodology.

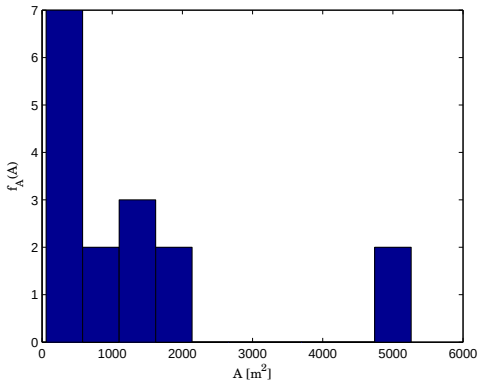

Figure 4.2: Histogram of the drainage areas at the channel heads in the Rio Col Duro basin, computed using the Dinf algorithm. The values of drainage area show a large variability, as they range between 110 $[m^2]$ and 5200 $[m^2]$ approximately.

The small values of contributing area at several channel heads (channel 2 up to channel 10, see Fig. 4.1) are explained by the formation of these tributaries not by a combination of flow accumulation and slope, but by subsurface flow in low slope areas, as previously explained in Section 4.1. Fig. 4.3 and Fig. 4.4 show examples of these two types of channel initiation processes observed in the Rio Cordon basin. In particular, Fig. 4.3 shows an example of channel head generated by erosion, while Fig. 4.4 shows a channel head generated by subsurface flow and very small slope.

This represents a challenge not only for the standard (global) channel extraction algorithms, but even for the geometric (local) methodology proposed by Passalacqua et al. [56], as a small threshold in the accumulation area is needed to further narrow the skeleton of likely channelized pixels, before the automatic detection of channel heads. In this case a threshold of 100 m^2 would be the maximum value allowed in order to

Figure 4.3: An example of channel head observed in the Rio Col Duro basin formed by a combination of flow accumulation and slope (*c13* in Fig. 4.1).

Figure 4.4: An example of channel head observed in proximity of the Rio Col Duro basin and formed by subsurface flow in a low slope area. The flow accumulation at channel heads of this type of channels can be of the order of just 100 m^2.

not interfere with the channel heads localization. In our application of the methodology proposed by Passalacqua et al. [56] we created a skeleton based on thresholding geometric curvature and slope-direction-change, as done in Lashermes et al. [26], and then we further narrowed it using a small contributing area threshold of 100 m^2. The introduction of the slope-direction-change criterion, as suggested by Lashermes et al. [26], is very useful in a basin like Rio Col Duro where the definition of a contributing area threshold for narrowing the skeleton is so challenging.

Now we focus on three small areas (T1, T2, and T3, respectively) indicated by the boxes in Fig. 4.1. The aim of this analysis is to test the two methodologies described above, in terms of their capability in detecting channel heads in areas with different morphology. The area T1 is taken as a test area for checking the suitability of the thresholds of positive curvature and slope-direction-change derived by the quantile-quantile plots for channel network extraction. The areas T2 and T3 are used to compare the performance of the two methodologies in detecting channel initiation with different surface morphologies: the area T2 is characterized by gentle slopes (mean slope value of 16°), while the area T3 by steep slopes (mean slope value of 30°) and the presence of a narrow valley.

4.2.1 Test area T1

Fig. 4.5 (a) and (b) show the quantile-quantile plots of curvature (Laplacian) and slope-direction-change, computed using as wavelets the first and second derivatives of the Gaussian kernel with appropriate variance such that the scale is approximately $a = 7m$, while Fig. 4.6 (a) and (b) show the corresponding plots for the geometric curvature and slope-direction-change computed through finite differences after performing 20 iterations (in time) of the Perona-Malik filter. It can be noticed by comparing Fig. 4.5 (a) with Fig. 4.6 (a) and Fig. 4.5 (b) with Fig. 4.6 (b) that the value of the standard normal variate z at which the deviation from normal and log-normal behaviors are observed (namely $z = 1$ for curvature and $z = 1.3$ for slope-direction-change), are methodology-independent, as expected since this value is representative of the statistical intrinsic behavior of the system, rather then the particular processing or the computational methodology employed.

After having identified the thresholds for the curvature and slope-direction-change,

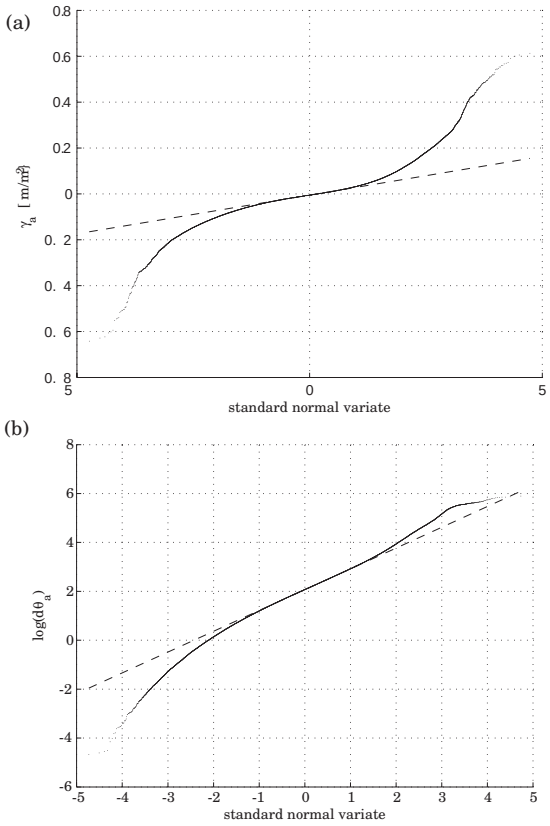

Figure 4.5: Quantile-quantile plot of the Laplacian computed with the Mexican hat wavelet with $\sigma = 2m$ which corresponds to $a = 8.9m$. The deviation from the normal behavior indicates a transition in the statistical behavior of the system. This transition here corresponds to a value of the standard normal variate $z = 1$ (a). Quantile-quantile plot of the slope-direction-change computed with the first derivative of the Gaussian with $\sigma = 1m$ which corresponds to $a = 6.28m$. The deviation from the normal behavior indicates a transition in the statistical behavior of the system. This transition here corresponds to a value of the standard normal variate $z = 1.3$ (b).

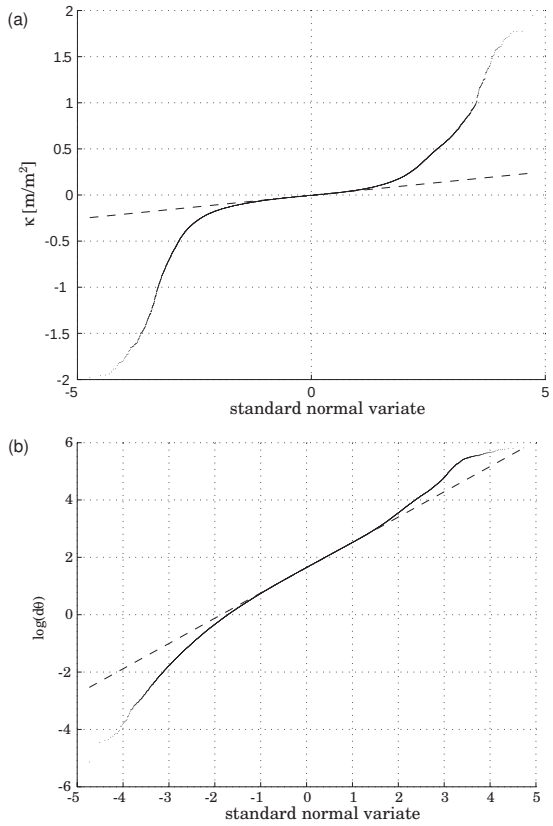

Figure 4.6: Quantile-quantile plot of the curvature computed through finite differences on the Perona-Malik filtered data ($t = 20$). The deviation from the normal behavior indicates a transition in the statistical behavior of the system. This transition here corresponds to a value of the standard normal variate $z = 1$ (a). Quantile-quantile plot of the slope-direction-change computed through finite differences on the Perona-Malik filtered data ($t = 20$). The deviation from the normal behavior indicates a transition in the statistical behavior of the system. This transition here corresponds to a value of the standard normal variate $z = 1.3$ (b).

we can extract the skeleton of the likely channelized pixels, as described in Chapter 3. Fig. 4.7(a) shows the skeleton of likely channelized pixels in test area T1, obtained through thresholding curvature and slope-direction-change computed through wavelets, as prescribed by the [26] methodology, at a scale of approximately $a = 7m$ (see Fig. 4.5). We can compare Fig. 4.7(a) with Fig. 4.7(b), obtained through nonlinear filtering after $t = 20$ iterations and thresholding curvature and slope-direction-change (see Fig. 4.6). We notice that both the skeletons identify appropriately channel initiation, but the skeleton obtained through nonlinear filtering, Fig. 4.7(b), shows less disrupted channels. In an area where no significative landslides are present, such as this one, as it can be seen from Fig. 4.1, channels are expected to be continuous.

While the wavelet methodology proposed by Lashermes et al. [26] does not perform an automatic detection of the channel heads, as the channels are traced in a semi-automatic fashion from the outlet to the sources, thus stopping at user's discretion, the geometric nonlinear methodology proposed by Passalacqua et al. [56] automatically detects channel heads, as described in Chapter 3. Before detecting automatically channel heads, a further noise reduction operation is performed introducing an additional threshold in the drainage area, here chosen equal to 100 m^2. This operation allows to obtain a narrower and more defined skeleton, as shown in Fig. 4.7(c), where the automatically detected channel heads are compared to the surveyed ones. It can be seen that the extracted channel heads are located just a few meters away from their actual localization.

4.2.2 Test areas T2 and T3

Fig. 4.8 (a) and (b) show the skeletons of likely channelized pixels obtained through thresholding curvature and slope-direction-change computed for the test area T2 through wavelets at scale a = 7 m (a), and computed through finite differences on the Perona-Malik filtered data after t = 20 iterations (b). Looking at these two figures one can observe that the channel recognition carried out with the finite differences on the Perona-Malik filtered data avoids the misclassification of 'noise', represented as isolated small convergence areas around the channel, as part of the skeleton of likely channelized pixels. The geometric approach gives better detection of the channels compared to the wavelet-based methodology.

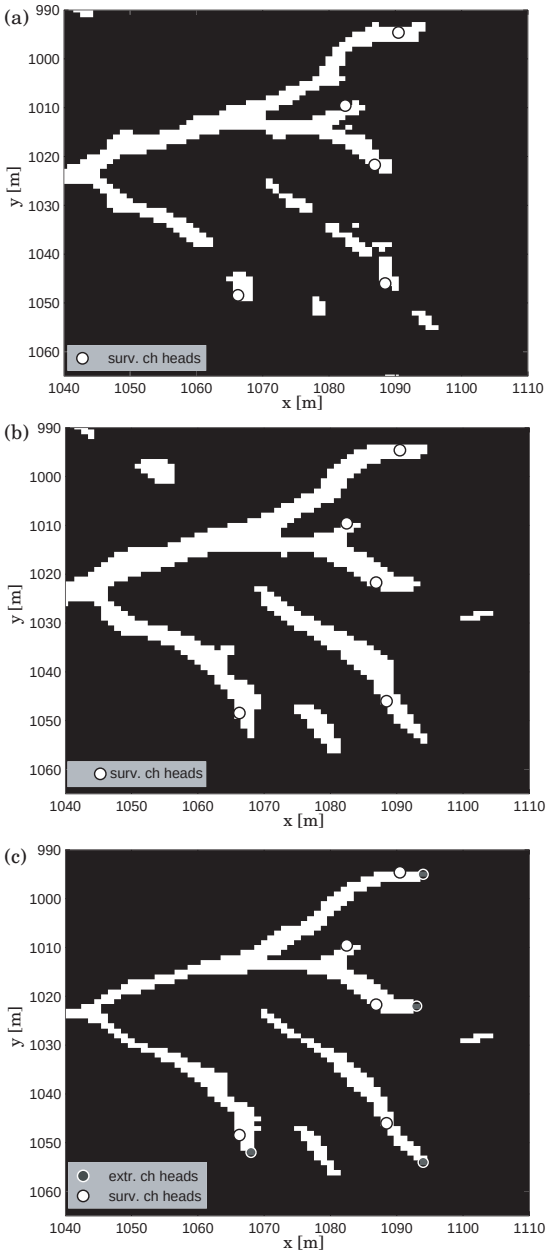

Figure 4.7: Test area T1. Skeleton obtained by thresholding curvature and slope direction change computed through wavelets at approximately $a = 7m$ (a). Skeleton obtained by thresholding geometric curvature and slope-direction-change computed through finite differences on the Perona-Malik filtered data after $t = 20$ (b). Skeleton obtained by thresholding geometric curvature, slope-direction-change, computed through finite differences on the Perona-Malik filtered data after $t = 20$, and drainage area. The figure shows the comparison between the extracted and the surveyed channel heads (c).

The results obtained in the test area T3 (Fig. 4.9 (a) and (b)) show that the two methodologies perform equally well. In this case, where steep slopes prevail and the valley is deeply incised, both methodologies recognize in detail the convergence areas without capturing at the same time the small convergence areas located nearby.

The different performance of the two methodologies in two different morphological areas addresses an interesting finding: where low slopes prevail the nonlinear filtering combined with finite difference computations employed in GeoNet result in more accurate extraction of channels compared to the wavelet-based methodology.

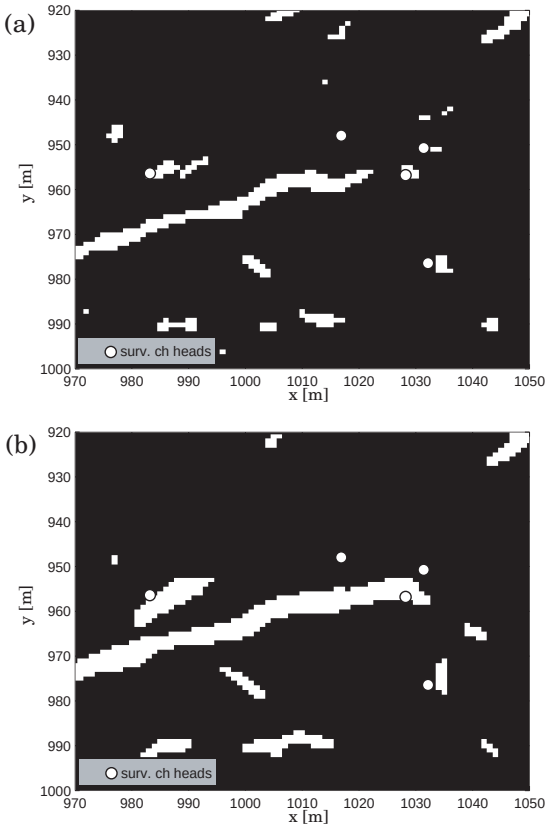

Figure 4.8: Test area T2. Skeleton obtained through thresholding curvature and slope direction change computed through wavelets at scale $a = 7m$ and surveyed channel heads (a). Skeleton obtained through thresholding curvature and slope-direction-change computed through finite differences on the Perona-Malik filtered data after $t = 20$ iterations and surveyed channel heads (b).

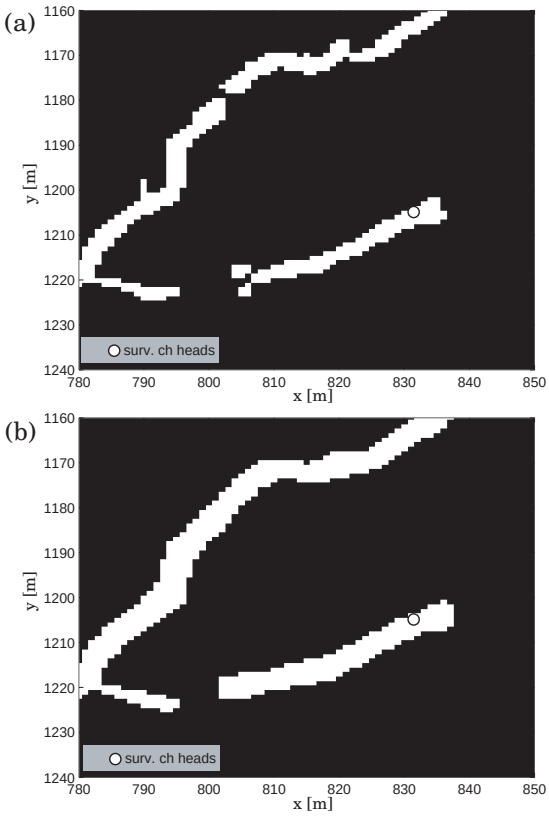

Figure 4.9: Test area T3. Skeleton obtained through thresholding curvature and slope direction change computed through wavelets at scale $a = 7m$ and surveyed channel heads (a). Skeleton obtained through thresholding curvature and slope-direction-change computed through finite differences on the Perona-Malik filtered data after $t = 20$ iterations and surveyed channel heads (b).

4.3 Channel disruption analysis

We now test the ability of the two methodologies in detecting channel disruptions corresponding to landslides. We focus this analysis on the black dotted rectangle ("landslide test area" in Fig. 4.1), located in the lower left part of the boundary (partly outside) of the Rio Col Duro basin. Fig. 4.10 (a) shows the skeleton obtained by thresholding curvature and slope-direction-change computed through wavelets, while (b) shows the same skeleton but obtained on the Perona-Malik filtered data and employing the geometric curvature. Both figures show also the location of several surveyed initiation areas of shallow landslides, here plotted in gray. Note the channel disruption correspondent to the largest landslide surveyed on the landscape (see *A* in Fig. 4.10). Both skeletons are interrupted at this location. In the other cases we can notice that the landslides are always located laterally with respect to the channel, and none of the channels overlaps an existing landslide. This shows that the thresholding criteria chosen serve the purpose of tracing the channels in the actual location, and identifying disruptions of interest. Both methodologies appear to be pretty successful, even though the wavelet based skeleton appears again a little more noisy and discontinuous. Also in this case the results are interesting since a classic global extraction method would have not been able to highlight the presence of these disruptions, as channels would be traced continuously throughout the basin with no possibility of detecting the presence of landslides.

4.4 Effect of linear versus nonlinear filtering on extracting channel cross-sections

We analyze in this section the effect of Gaussian filtering versus nonlinear Perona-Malik filtering on extracting channel cross sections in the Rio Col Duro basin. In particular, as it can be seen in Fig. 4.1, we extracted three cross-sections, one in the colluvial channel within a gentle slope area (labeled as *CS1* in Fig. 4.1), one in the bedrock channel (labeled as *CS2* in Fig. 4.1) and the third one in the alluvial channel (labeled as *CS3* in Fig. 4.1). Fig. 4.11 (a) through (c) show the original cross-section and the ones cut after performing Gaussian or nonlinear filtering on the elevation data. In the case of Gaussian filtering we have used two smoothing scales, namely $\sigma = 1m$,

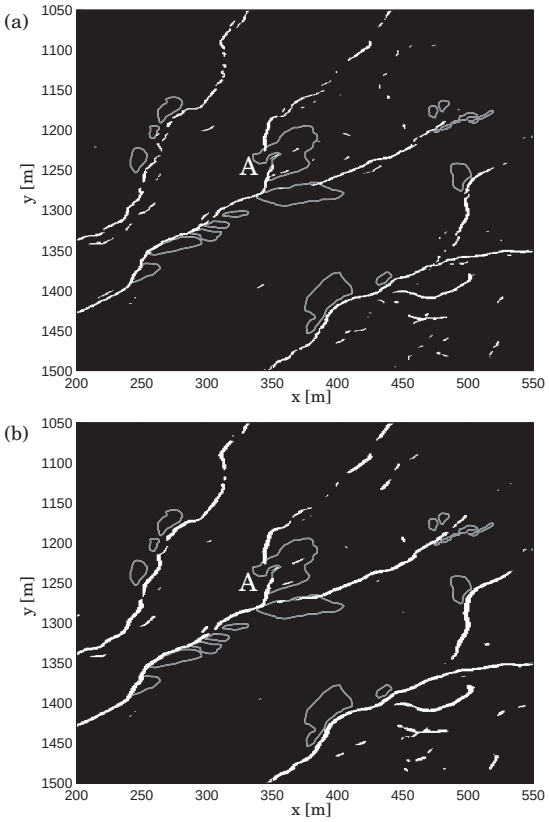

Figure 4.10: Skeleton obtained by thresholding curvature and slope direction change computed through wavelets at approximately $a = 7m$ and surveyed landslides (gray contour patches). Note the disruption in correspondence to the largest landslide, indicated as A, as observed in the field (a). Skeleton of likely channelized pixels obtained by thresholding geometric curvature and slope-direction-change on the Perona-Malik filtered data and surveyed landslides (gray contour patches). Note the channel disruption in correspondence to the largest landslide, indicated as A, as observed in the field (b).

which corresponds to $a = 4m$, and $\sigma = 7m$, which corresponds to $a = 28m$. For the nonlinear filtering we have performed 20 and 50 iterations. In all the three cross-sections, thus independently of the local geological characteristics, we can notice how Gaussian filters of increasing scale tend to shift more and more the centerline of the channel and also lower the elevation of the landscape. Furthermore, increasing the scale, the cross-sections become increasingly smoothed, and in particular in the case of cross-section 2 (colluvial channel) the left bank of the channel ends up disappearing. This has an effect on the channel extraction itself, resulting in increasingly disrupted skeletons of likely channelized pixels, even in areas with no landslides present. Thus it is concluded that nonlinear filtering of landscapes offers advantages for both channel network extraction and extraction of cross-sections.

Looking at the three figures it is also interesting to note how clear is the different morphology of the colluvial channel cross-section compared to the bedrock and alluvial ones. Bedrock and alluvial channels are deeply incised and are located in the steep slope area of the Rio Col Duro basin, while the colluvial channel presents shallow incision and smoothed topography. This channel is located in the gentle slope area of the basin, where the employment of nonlinear filtering is recommended.

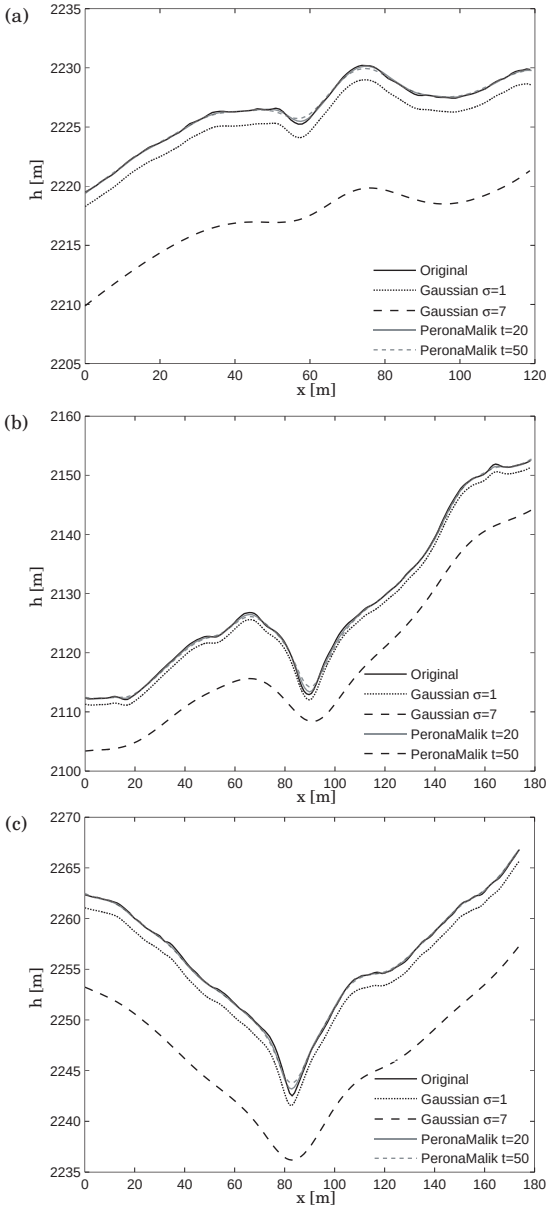

Figure 4.11: Cross-sections cut in the Rio Col Duro basin. Colluvial channel *CS1* (a), bedrock channel *CS2* (b) and alluvial channel *CS3* (c).

Chapter 5

Geomorphic Feature Extraction Methodologies in Flat Areas

The Le Sueur river basin is a major source of sediment to the Minnesota river. Due to the very high turbidity levels in Lake Pepin, management decisions are needed to reduce sediment loads. Thus the identification of sediment sources in the Le Sueur river is of primary importance. For this purpose, research has been extensively conducted using a combination of digital elevation data, gauging station observations and air photos, as described in Gran et al. [2]. Also a hydrologic and sediment routing model is being currently developed within which existing observations can be interpreted and future predictions can be made under various management scenarios. In such modeling efforts, the location of terrain features such as terraces, dikes, bluffs etc., need to be explicitly specified. Typically, this is done by hand-digitization of maps and manual specification of the coordinates of such features. Other terrain features of importance in modeling studies are: the centerline of the channel (not well resolved due to the poor reflectance properties of water), the heights of bluffs, and the elevation difference between left and right banks of streams (an important parameter in computing sediment loads to the system). Also, the distinction of artificial versus natural channels is of great interest, as agricultural ditches represent a substantial source of sediment into the system.

In this chapter, we propose a technique for the automatic extraction of channel cross-sections, the automatic detection of banks locations, the identification of water

surface elevation, and the estimation of bluff heights. We show how natural and artificial features (channels and ditches) imprint a different signature on the landscape, which can be used to distinguish them. We also explore the challenges encountered when applying the geometric channel extraction methodology described in Chapter 3, developed on a steep landscape such as the Eel River basin in northern California, to a flat landscape, such as the basin of the Le Sueur river in Minnesota.

5.1 Study area

The Le Sueur river is located in south-central Minnesota and it covers an area of 2880 km^2 of which 87% is employed for agriculture. The Le Sueur river drains north and west to the Minnesota river (see Fig. 5.1) and modern sediment-gauging measurements have indicated that, despite the fact that the Le Sueur watershed area constitutes about 7% of the total area covered by the Minnesota river, it provides $\sim 24\% - 30\%$ of the total suspended solids (TSS) entering the Minnesota river. The Minnesota river is, in turn, the major source of sediment for Lake Pepin, whose turbidity levels are so high to require management decisions on how to reduce sediment loads. Thus an understanding of the sediment source locations and of the transport processes for sediment entering the Minnesota river is of primarily importance for helping restoring clean water and improving the ecosystem functionality in the Minnesota river and Lake Pepin.

Rapid base-level fall at the outlet of the Le Sueur river $11,500$ yr B.P. triggered up to 70 m of channel incision at the mouth. Knickpoints have migrated $30 - 35$ km upstream on all the three major branches of the river. The basin results divided into two parts: the upper watershed, above the knick points, which receives sediment primarily from uplands and streambanks, and the lower zone, below the knickpoints, which receives also substantial inputs from bluffs and ravines.

5.2 Methodologies used and possible improvements

We provide here a summary of the analysis carried out so far by a group of researchers involved in the Le Sueur project and the methodologies employed to identify the sediment source locations in the Le Sueur River. More information regarding the area and

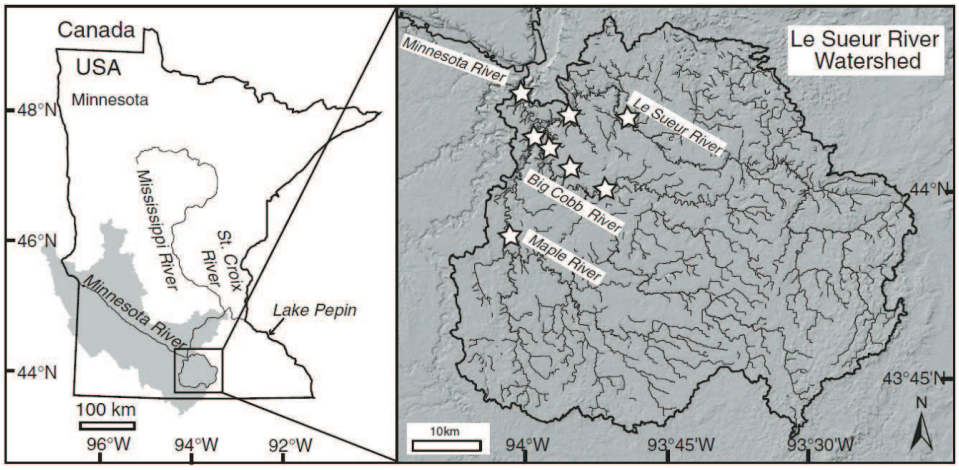

Figure 5.1: Location map the Le Sueur river basin. Figure from Gran et al. [2].

the project can be found in Gran et al. [2]. The analysis performed has used a combination of digital topography (including high resolution topography acquired through LiDAR in spring 2005), gauging stations data (located above and below the knick zones on the major tributaries) and historical air photos from 1938 to 2003. The digital topography data set covers $\sim 30\%$ of the total watershed area. Most of the analysis performed includes the hand-digitalization of features such as ravines, channel banks, terrace surfaces, etc. This adds variability to the resulting computation of the difference in elevation among the channel banks and in measuring bluffs height. In addition, few data points were collected in the channel due to the poor reflectance properties of the water. During pre-processing a water surface was interpolated from the exposed channel banks, resulting in a 'lumpy' water surface, which results in a noisy channel elevation profile. Another point of interest, missing in the current analysis, is the possibility of identifying the connectivity of agricultural fields to the drainage network. This operation is critical to understanding terrestrial sediment transport. Common watershed delineation techniques typically fill internal sinks within a watershed, based on the assumption that these internally drained regions are a result of error on the vertical data, but this assumption is not necessarily valid in low relief landscapes.

We found this data set and the project itself of interest for testing the capability of the geometric methodology in extracting the river network in such a flat area and

also we saw the possibility of expanding the methodology to the automatic extraction of channel morphology properties and other terrain features.

5.3 Automatic detection of cross-sections, channel banks, water surface elevation, and bluff heights

5.3.1 Automatic extraction of channel cross-sections

We focus this part of our analysis on a 25 km^2 tributary of the Le Sueur river, shown in Fig. 5.2. The first step of our analysis is to extract its river network. Following the steps prescribed in the application of the geometric feature extraction methodology described in Chapter 3, we compute the curvature and the slope-direction-change and we obtain the corresponding quantile-quantile plots. The difference between this application of the methodology to the one presented in the previous chapters, is that we employ the Laplacian as definition of curvature instead of the geometric one. This choice is explained by looking at Fig. 5.3 which shows the geometric curvature in (a) and the Laplacian in (b). While the landscapes analyzed in the previous chapters were characterized by the presence of natural features only, this data set includes roads and artificial ditches in addition to natural channels. The geometric curvature, as previously defined in (3.1), because of the normalization by the gradient magnitude, allows the curvature to be of about the same order of magnitude throughout the area, thus making it easier to detect the channels. In the case of the Le Sueur river basin, this normalization operation highlights the presence of every other feature, other than channels, thus making the extraction of channels more challenging. As shown in Fig. 5.3 (b), instead, the Laplacian acts as a more 'selective' measure of curvature, resulting in a better defined image of the topography.

After the computation of curvature and slope-direction-change, we plot the quantile-quantile plots to find the values of the standard normal deviate corresponding to the transitions from hillslope to valley (from the quantile-quantile plot of curvature) and from valley to channel (from the quantile-quantile plot of slope-direction-change). Fig. 5.4 shows the quantile-quantile plot of the Laplacian curvature (a) and the quantile-quantile plot of the slope-direction-change (b). Both transitions correspond to a value of the

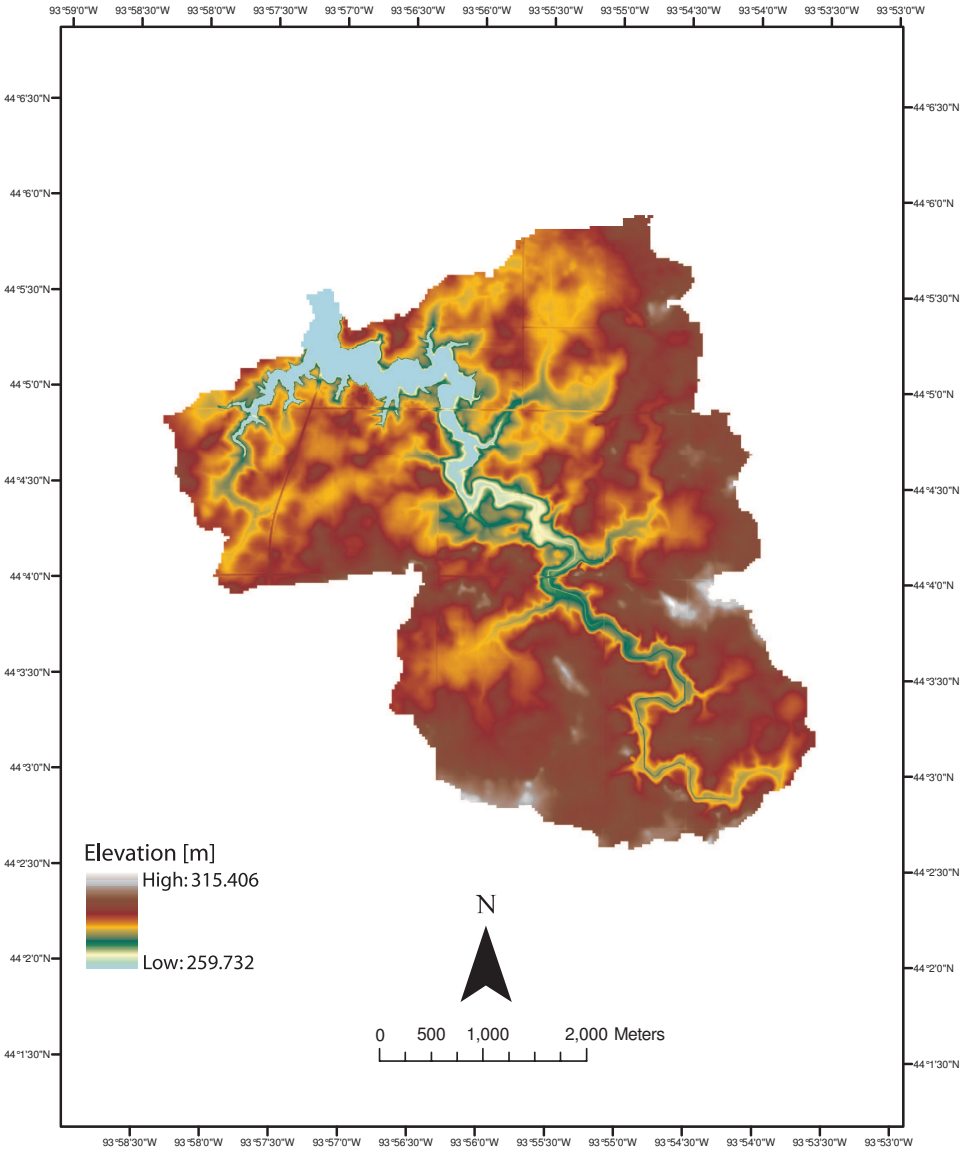

Figure 5.2: Location map of a 25 km^2 tributary of the Le Sueur river.

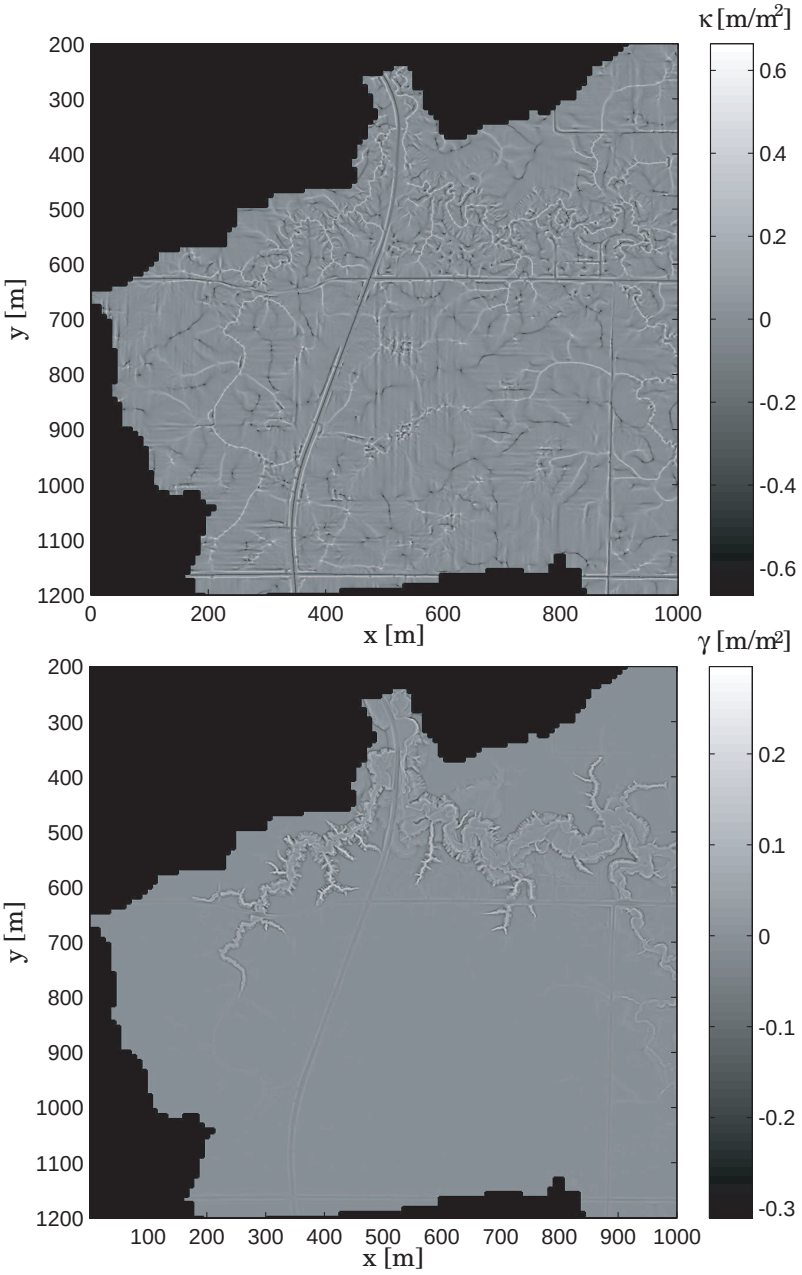

Figure 5.3: Curvature computed on the Le Sueur tributary (shown only in part of the basin to make it visually clear). Geometric curvature (a). Laplacian (b).

standard normal deviate $z = 1$.

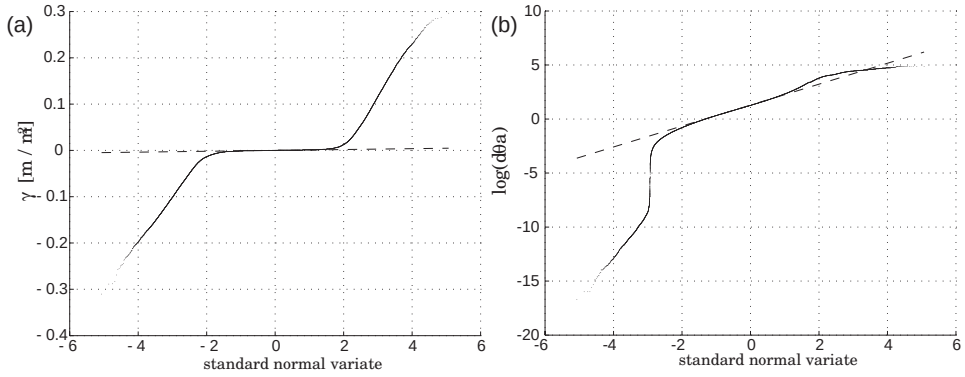

Figure 5.4: Quantile-quantile plot of the Laplacian for the Le Sueur tributary. The value of the standard normal deviate which corresponds to the transition from hillslope to valley is $z = 1$ (a). Quantile-quantile plot of the slope-direction-change for the Le Sueur tributary. The value of the standard normal deviate which corresponds to the transition from valley to channel is $z = 1$ (b).

Using the two thresholds obtained from the quantile-quantile plots we have obtained the river network shown in Fig. 5.5. In this application, as for the one presented in Chapter 4, the naturally emerging threshold in slope-direction-change avoids the need to select a subjective threshold in the contributing area as a further 'noise reduction' operation.

Now that we have obtained the river network of the Le Sueur tributary, we focus on the main stem to illustrate the procedure for extracting automatically channel cross-sections and channel morphology. Fig. 5.6 (a) shows an example of a river transect along which the cross-section is extracted. The way the transect is traced is explained below. Let us assume we want to extract the cross-section at location (x_1, y_1) along the main channel. First we can compute the vector between location (x_1, y_1) and the immediate upstream (or downstream) location along the main channel, which we can indicate as (x_2, y_2). From vector algebra, the vector connecting these two points is given by:

$$\vec{r} = (x_2 - x_1)\vec{i} + (y_2 - y_1)\vec{j} \tag{5.1}$$

After obtaining the vector $\vec{r}$, we can compute the orthogonal vector $\vec{q}$ as:

$$\vec{q} = (-r_2)\vec{i} + (r_1)\vec{j} \tag{5.2}$$

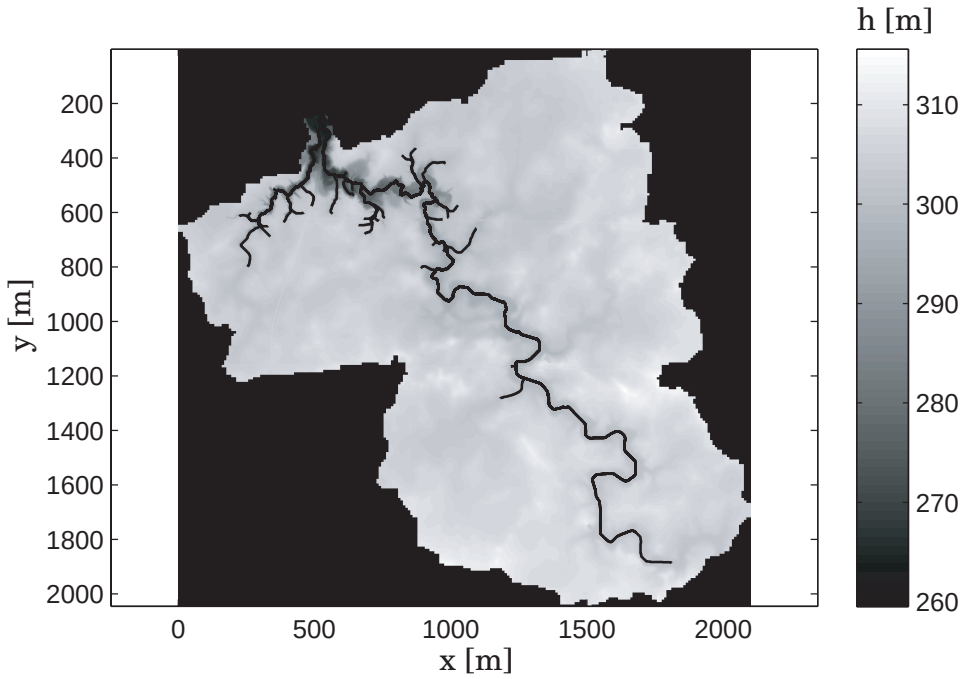

Figure 5.5: Extracted river network for the Le Sueur tributary.

Then, the unit vector is obtained by:

$$\hat{e} = \frac{\vec{q}}{|\,\vec{q}\,|} \tag{5.3}$$

where $|\,\vec{q}\,|$ is the magnitude of the vector $\vec{q}$. We perform the above steps using more than one location upstream and downstream of the cross-section location to take into account the sinuosity of the channel.

The coordinates (x, y) of a transect of 180 m (90m on each side of the centerline), for example, are obtained by multiplying a vector $[-90, 90]$ by the components of the unit vector $\hat{e}$. Fig. 5.6 (a) shows an example of transect orthogonal to the main stem of the Le Sueur tributary extracted with the procedure described above. To extract the channel cross-section we simply have to plot the topographic data corresponding to the transect orthogonal to the channel. Fig. 5.6 (b) shows the cross-section correspondent to the transect shown in Fig. 5.6 (a). This particular shape of the cross-section (note the levees on the banks of the channel) is typical of the upstream part of the Le Sueur tributary which is used as a drainage ditch.

Our goal now is to develop a methodology for extracting automatically the channel banks and the water surface elevation. If we look at the banks of the channel, we can notice a dramatic change in slope. In particular, we expect the slope to be maximum along the 'walls' of the channel and then lower at the adjacent terraces. The plot of the slope along the cross-section, as in Fig. 5.6 (c), shows the presence of two peaks, one on each side of the channel, indicating the location where the slope is largest just in proximity of the channel banks. This information can be used to identify the water surface elevation and the location of the channel banks as follows. First, we identify the peaks of the slope and we take into consideration only the ones within 25 m on each side of the centerline. The 50 m range was defined based on the fact that we know the channels on this basin to be $20 - 30$ m wide. Then, among the two maximum peaks on each side, we pick the minimum one as the one corresponding to the lower bank, thus the one defining the water surface elevation. The minimum peak is chosen as the one corresponding to the less steep bank, thus more likely to be the lower among the two banks.

Once the water surface elevation has been identified, we determine the location of the other bank as the point at which the water surface elevation projects to the channel bank on the other side with respect to the channel centerline. Fig. 5.6 (d) shows the cross-section at the location indicated in Fig. 5.6 (a) after tracing the water surface elevation.

The operation described above can be automatically repeated for each cross-section along the Le Sueur river networks and the resulting water surface elevation can be used for the computation of an energy slope along the channels.

5.3.2 Automatic identification of bluff heights

The height of the bluff is a good surrogate for the amount of incision since the channel last occupied this position. If we define as $\Delta\eta$ the difference in elevation between the eroding and the depositing sides of the channels, then for a river that is incising vertically much more rapidly than it is migrating laterally, $\Delta\eta$ should be high and the proportion of the river that is eroding into a tall bluff should be high. For a river that is migrating laterally at a rate much faster than it is incising, instead, the $\Delta\eta$ value should be much smaller and the river tends to be dominated by floodplain deposition

rather than incision. In such a system the proportion of the river that is eroding into a tall bluff should be low. There is a lot of interest in establishing the behavior of the Le Sueur river, whether it is vertical incision or lateral migration the dominant process and this can be obtained through a plot of the probability of exceedance of $\Delta\eta$. Of course the correct computation of the bluff height is really important towards achieving this goal. For this reason, and taking advantage of the methodology described above for automatically detecting the locations of the channel banks, we suggest to compute $\Delta\eta$ as the difference between the elevations corresponding to the left and the right bank. Values of $\Delta\eta$ greater than $3m$ will then be considered bluffs, as this is the order of magnitude of these features in the Le Sueur basin. This analysis has not been performed as part of this work but it is an issue of future research.

5.4 The signature of natural versus artificial features: distinguishing between channels and ditches

Artificial drainage ditches, either intermittent or perennial, constitute an important part of the Le Sueur river network and an important source of sediment into the system. The distinction between artificial and natural channels is an important step towards identifying the major sediment sources of the basin. Although generally more linear than natural channels, artificial ditches have been often designed on top of natural channels, making their identification very challenging to the naked eye. As shown in Fig. 5.6 (b), the ditch cross-section presents very well defined levees; furthermore we expect less variability in the curvature along an artificial ditch, then along a natural channel.

We focus this analysis of the signature of artificial versus natural features on part of the Maple basin, tributary of the Le Sueur and located South-East of the tributary analyzed in the previous section. Fig. 5.7 shows the area in analysis and the surveyed data available. In particular, the white continuous line represents natural channels, while the dotted white line indicates artificial ditches. As observed in the previous section and shown in Fig. 5.3, the Laplacian seems to be a more appropriate measure of curvature than the geometric one for this area. Thus, we compute the Laplacian for this data set and plot the quantile-quantile plot, as shown in Fig. 5.8.

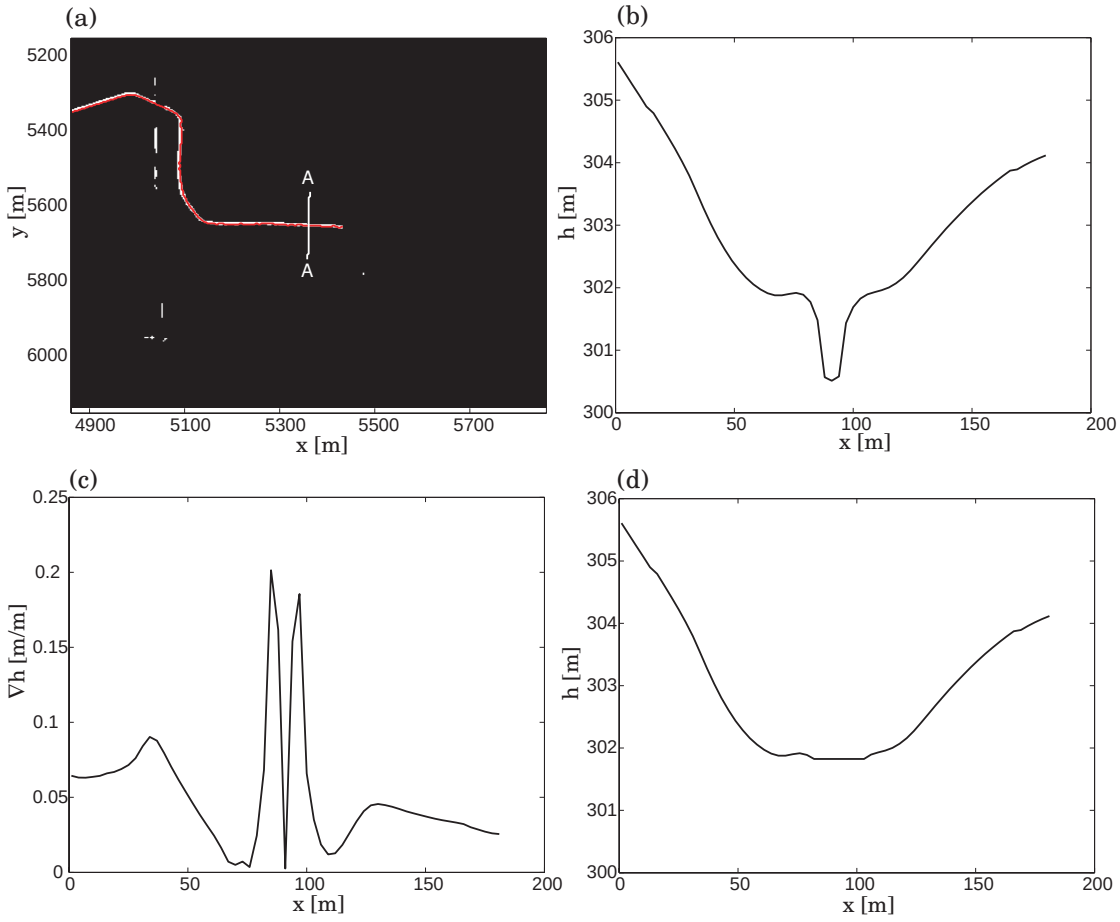

Figure 5.6: 180 [m] transect A-A cut perpendicularly to the main stem of the Le Sueur tributary (a). Cross-section of the Le Sueur tributary along transect A-A (b). Slope of the Le Sueur tributary along transect A-A (c). Cross-section of the Le Sueur tributary along transect A-A after tracing the water surface evelation (d).

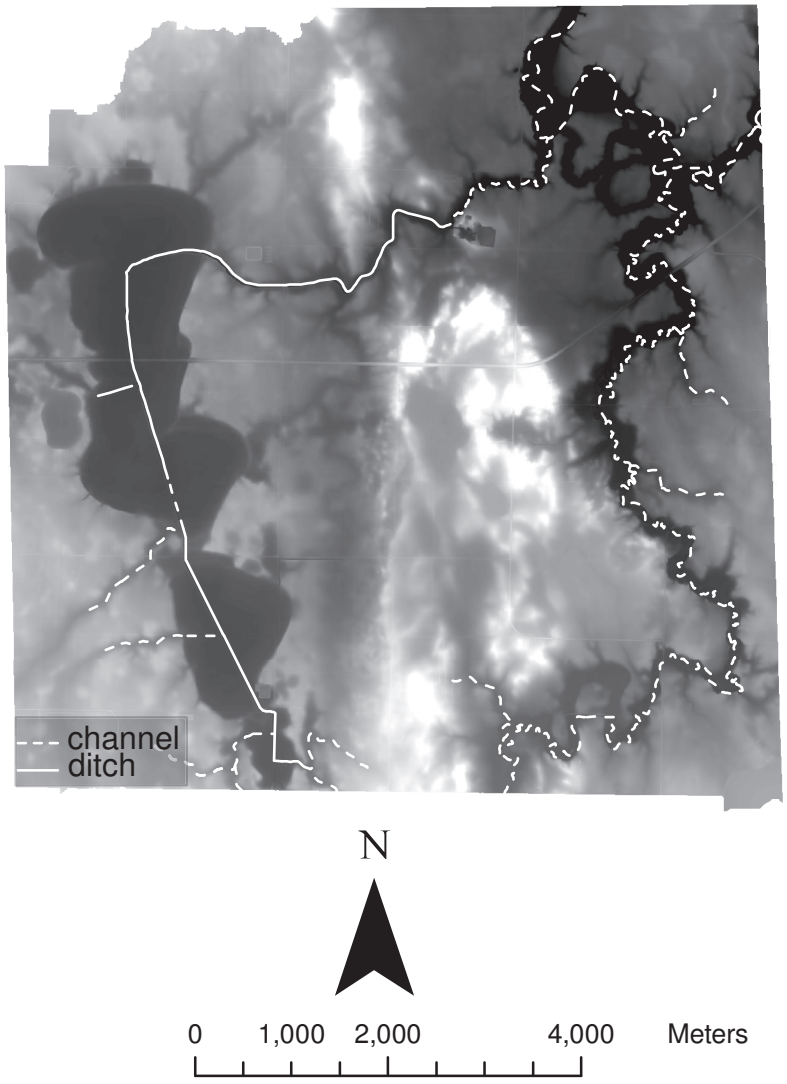

Figure 5.7: Part of the Maple river where we focus the analysis of the signature of artificial versus natural features. The white continuous lines indicate natural channels, while the dotted white lines represent artificial ditches.

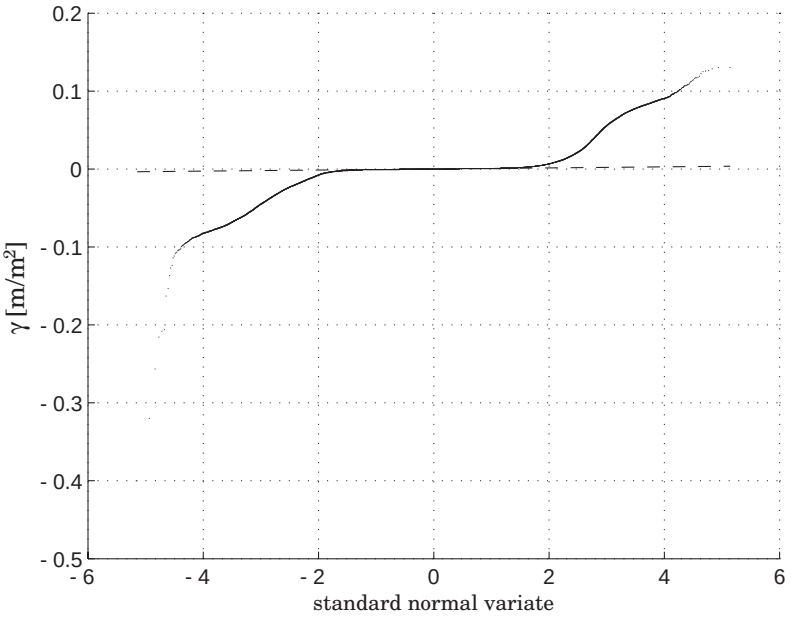

Figure 5.8: Quantile-quantile plot of the Laplacian curvature for part of the Maple basin in analysis, and shown in Fig. 5.7.

This time, we focus on the very convergent pixels, as we expect the artificial ditch, because of the presence of the levees, to show higher values of Laplacian curvature and less variability. Fig. 5.9 shows the skeleton obtained after imposing a curvature threshold corresponding to the standard normal deviate $z = 5$. This value of the standard normal deviate was determined from the quantile-quantile plot in Fig. 5.8 as corresponding to the very convergent pixels, which are the ones we expect to belong mainly to the ditch, because of its well defined levees. As it can be seen, the skeleton appears to be mostly continuous along the artificial ditch. Applying the geodesic minimization principles, we can extract the ditch only, obtaining what shown in Fig. 5.10.

5.5 Challenges, opportunities and further research

We have seen how the geometric geomorphic feature extraction methodology developed in a steep landscape, such as part of the Eel River basin in Northern California, applies well to a flat area such as the Le Sueur basin in Minnesota. In particular, as also discussed in Chapter 4, the application of a nonlinear filter instead of a linear one

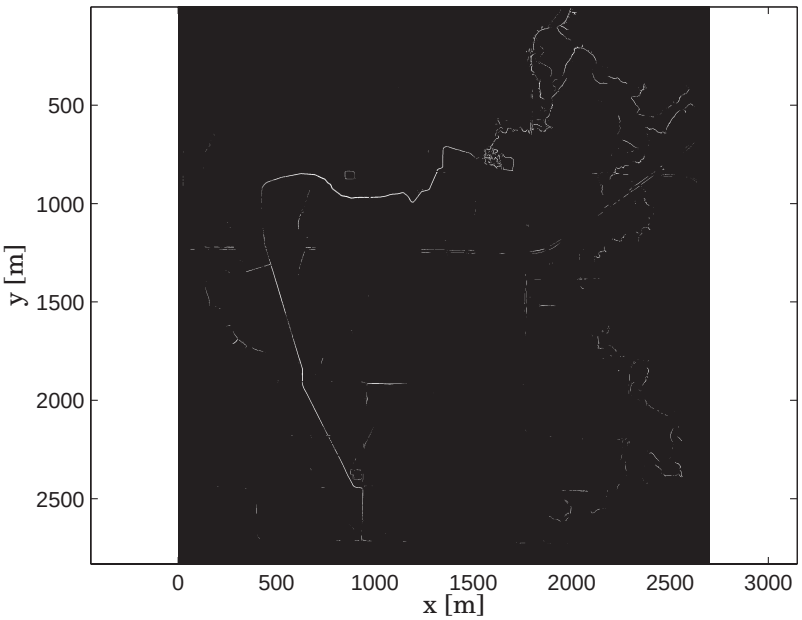

Figure 5.9: Skeleton of the Laplacian curvature obtained with a threshold $z = 5$ of the standard normal deviate.

becomes crucial when low slopes prevail. In addition, the global extraction approach through geodesic curves, allows to perform efficiently the channel extraction operation without being affected by sinks and roads and the presence of bridges that cross the river network. Using a classic extraction methodology, based for example on area threshold, the bridges have to be removed manually and the elevation at those locations replaced by an interpolation of the elevation at the surrounding locations. The global approach through geodesic curves, instead, achieves the connection of channel heads to the basin outlet, without being affected by missing data.

The use of a minimal area threshold, that we proposed in our first application of the geometric feature extraction methodology to further process the data eliminating occasional isolated convergent pixels, does not seem to be ideal in this data set. Instead, the combination of a threshold in curvature and a threshold in slope-direction-change seems to achieve good results.

The methodology proposed to automatically extract cross-sections, bank locations, water surface elevation and bluffs height, should improve the ongoing analysis performed

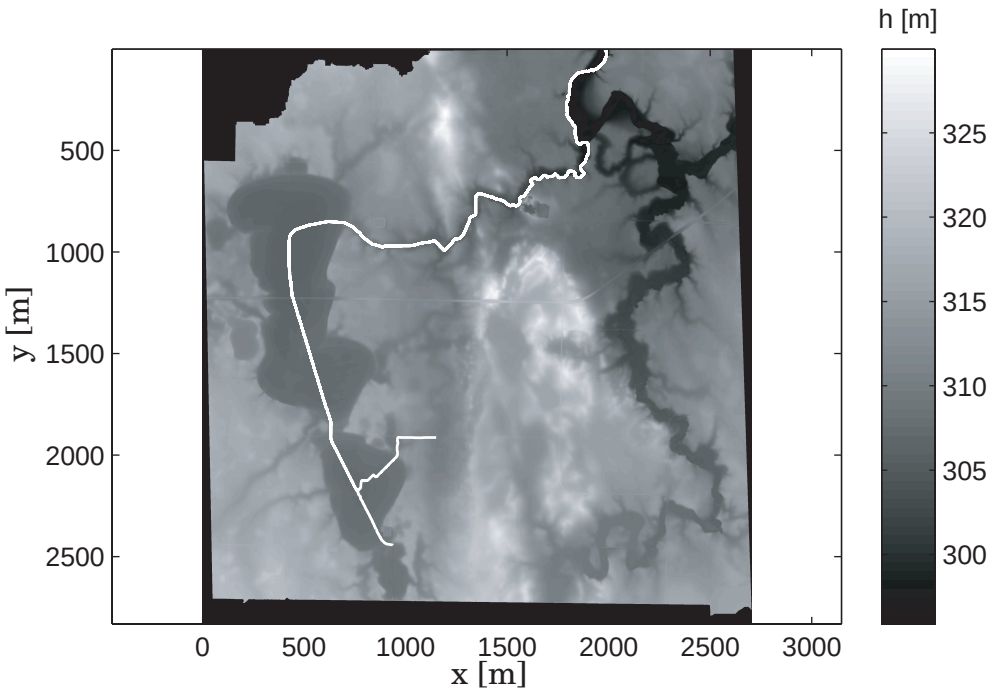

Figure 5.10: Artificial ditch extracted from the skeleton of Laplacian curvature with $z = 5$.

in the area with the final goal of identifying sediment sources. The automatic detection makes the extraction of these quantities not only efficient and fast, but also more objective, as the user does not have to visually identify them and digitize them manually.

Although strongly supported by the analysis shown in Chapter 3, the use of the geometric curvature does not seem to be appropriate in the Le Sueur data set. The normalization through the gradient magnitude, fundamental to enhance features in a steep and natural channels, makes the extraction more difficult in a landscape such as this one, where natural and artificial features are present. The Laplacian, instead, seems to be a more selective measure of curvature. In particular, we have found the Laplacian a fundamental quantity to capture the different signature of artificial ditches from the one of natural channels.

Chapter 6

A Non-local Fluvial Erosion Model

Geomorphic transport laws, which form the foundation of landscape evolution models, can be written as expressions of the sediment flux as a function of the local slope at the point of interest, and a bulk expression of the upstream influence typically via the upstream contributing area. Recently, the hypothesis of a non-local sediment flux which is explicitly informed by the details of the upstream contributing area, e.g., slopes of the upstream flowpaths and the heterogeneity of sediment-producing mechanisms which move sediment over a wide range of distances downslope, has been investigated in order to explain steady-state hillslope profiles (e.g., see Foufoula-Georgiou et al. [65] and Tucker and Bradley [66]).

In the context of landscape evolution, Benda and Dunne [67, 68] proposed a model for taking into account the effect of variability in sediment supply to a river network. In particular, the model was applied to the Oregon Coast Range, in which the sediment supply to channels comes from landslides and debris flows. The model of Benda and Dunne [67, 68], thus, acknowledged the effect of upstream processes (such as a landslide or a debris flow) on the flow in the river network, thus taking into account the non-locality of processes acting in nature. In this chapter we explore a non-local formulation of fluvial erosion and study the statistical properties of the steady-state landscapes it produces. The non-locality in this case is taken into account through a

fractional formulation, which consists into a convolution of slopes with a kernel which gives decreasing weights as upstream distance from the location of interest increases. We report surprising similarity of the modeled landscapes to the ones obtained with a previously proposed nonlinear model [25] and put forth the hypothesis that non-local transport laws (which are linear) can give rise to channel-dissected landscapes typically reported to arise only from nonlinear sediment flux formulations (see, e.g., Birnir et al. [69]).

6.1 Landscape evolution modeling

The understanding of how landscapes are created and the development of models able to reproduce appropriately their characteristics, has been a subject of research for many years. Starting with the early work of Culling [3], several models have been proposed with the idea of reproducing certain landscape properties. Following the distinction between modeling approaches proposed by Dietrich et al. [23], models can be focused on making short term predictions for specific features, e.g., river grain size, river bed depth (*detailed realism*); on large-scale predictions tested only on the appearance of the outcome, as knowledge of finer scale mechanisms is lacking due to computational restrictions (*apparent realism*); on reproducing statistical properties of the system emerging at steady-state (*statistical realism*); and finally on explaining quantitative relationships, parameterizing models in terms of field measurements and observations (*essential realism*).

All the approaches mentioned above have had an important role in understanding how landscapes are formed. Most of the models proposed require an assumption of a transport law and boundary conditions and then the solution of conservation of mass over an initially random field until steady-state is reached. Recent efforts have also shown the opportunity of using high resolution topography as initial condition (see, e.g., Dietrich et al. [23] and Roering [70]).

A particular class of models aiming at the analysis of the statistical properties of steady-state landscapes (*statistical realism*) was derived starting from the so-called Kardar-Parisi-Zhang (KPZ) equation. This equation, originally proposed in the physics community to study the growth of atomic interfaces by ion deposition [71], inspired a

class of landscape evolution models, created with the specific idea of studying coarse-grained properties of landscapes [72, 73, 74]. Furthermore, the connections between the KPZ model to turbulence (under a simple transformation of variables, the deterministic KPZ equation takes the form of the Burgers equation, a low-dimensional analog to the Navier-Stokes equation) has suggested the possibility of parameterizing the effect of subgrid-scale fluxes through techniques used in Large-Eddy-Simulation (LES) of turbulent flows in atmospheric sciences [25].

Taking advantage of the nonlinear numerical model developed by Passalacqua et al. [25], we now would like to question whether the fluvial patterns observed as an outcome of landscape evolution models are necessarily produced by the nonlinearity in the model, as usually assumed (see, e.g., [69]). In particular, inspired by recent advances in the inclusion of non-locality in the context of hillslope transport through fractional formulations, we are interested in analyzing the patterns that a linear non-local formulation of landscape evolution would give rise to, and in comparing its steady-state results to the ones obtained by Passalacqua et al. [25] with the nonlinear model, as well as patterns of real landscapes.

6.2 Proposed model: Fractional diffusion

Here we first recall the derivation and resulting form of the nonlinear model used by Passalacqua et al. [25] and then we introduce our new non-local formulation for fluvial erosion.

The Kardar-Parisi-Zhang equation is given by:

$$\frac{\partial h}{\partial t} = D\nabla^2 h + C \mid \nabla h \mid^2 + \eta \tag{6.1}$$

The right hand side of (6.1) includes a diffusion term (most left term), where D is the diffusion coefficient, a nonlinear term, where C is a constant and ∇h is the slope (middle term), and a white noise term (most right term). Neglecting the noise term and the diffusion term, as assumed to be effective only at small scales, (6.1) is left with only the nonlinear term on the right hand side. Taking into account that the process of erosion is coupled with the water flux acting on the surface, the constant C can be written as the product of an erosion coefficient α and the water flux q. The governing equation

thus becomes (with the addition of a constant uplift U):

$$\frac{\partial h}{\partial t} = U - \alpha q \mid \nabla h \mid^2 \tag{6.2}$$

Equation (6.2) is a special case of the general unit stream power model given by (again with the addition of a constant uplift U):

$$\frac{\partial h}{\partial t} = U - \alpha A^m \mid \nabla h \mid^n \tag{6.3}$$

The nonlinear model in (6.2) is thus given by (6.3) for the particular case of $m = 1$ and $n = 2$, which agrees with the condition $\frac{m}{n} \sim 0.5$ typically assumed for a detachment limited system [75, 76, 77] such as the one simulated by Passalacqua et al. [25]. We recall here that a detachment-limited system differs from a transport-limited system as in the latter the stream will incise if and only if the local transport capacity of the stream is greater than the sediment load supplied from upstream [78], while in a detachment-limited system the rate of incision is determined by the ability of the stream to erode the bed and the sediment transport capacity exceeds the sediment flux. Thus in (6.2) it is assumed that all the material that is removed from the bed is transported and washed away, without any deposition.

We propose the following non-local formulation:

$$\partial_t h = U - cA\nabla_x^\alpha h \tag{6.4}$$

where $\nabla_x^\alpha h$ denotes the α-order fractional derivative of $h(x)$ and α is the so-called *degree of non-locality* which varies between 1 and 2. It is noted that for $\alpha = 2$ (6.4) is simply a linear diffusion model which at steady-state ($\partial_t h = 0$) would result in a smooth landscape of parabolic shape ($\nabla_x^2 h(x) = const$).

Fractional derivatives are an extension of integer order derivatives (e.g., [79]). The two most common definitions of a fractional derivative are the Riemann-Liouville (6.5) and the Caputo (6.6) forms:

$$\frac{d^\alpha h}{dx^\alpha} = \frac{d^n}{dx^n}(I^{n-\alpha} h(x)) \tag{6.5}$$

$$\frac{d^\alpha h}{dx^\alpha} = I^{n-\alpha}\left(\frac{d^n h(x)}{dx^n}\right) \tag{6.6}$$

where n is an integer such that $n-1 < \alpha < n$ and $I^{n-\alpha}(\cdot)$ is the fractional integration operator of order $n-\alpha$. For $1 < \alpha < 2$, (6.4) emulates a super-diffusion (faster than normal diffusion transport) [80]. In the preliminary simulations reported here we have chosen a value of $\alpha = 1.5$, although future work will cover the full range between 1 and 2. We explain in the following section the numerical set-up and how the computation of the fractional derivative is performed.

6.3 Numerical simulations

The numerical setting used in the simulations is the same used by Passalacqua et al. [25]. Under the assumption of uniform rainfall acting on the surface, the water flux at a given point is proportional to the area draining at that location. The steady-state configuration depends on the external conditions applied to the problem. If the boundary condition at the output is a fixed elevation with constant uplift, then steady-state is reached when the erosion rate balances the rock uplift over the whole system [81, 82, 13, 73, 83]. If the uplift rate is zero, the system reaches a steady-state when nearly all the material has been eroded [84]. The initial condition is a sloping surface obtained by [73, 25]:

$$h(x, y, t = 0) = s_0 \cdot [y + dy \cdot rand(x, y)] \tag{6.7}$$

where h is the elevation, s_0 the initial slope, y the pixel coordinate, dy the grid resolution, and *rand* a uniform random number in the range $[0, 1]$. This initial configuration prevents the formation of lakes during the evolution of the field to steady-state. The boundary conditions are: an infinite wall at the upstream end of the field; an output boundary at fixed height equal to zero and located at the downstream end of the field, and on the lateral sides the flow is forced to drain into the system and cannot drain outside of it. For the computation of the slope we use the steepest descent algorithm: at every location the elevation is compared with the one of the eight surrounding neighbors and the local slope is assumed as the one to the lowest neighbor. Once we have the local slope computed, the fractional derivative of h of order α is given by the Grünwald formula [85]:

$$\frac{d^\alpha h}{dx^\alpha} \simeq \sum_{k=0}^{N-1} \frac{1}{\Delta x(k)^{\alpha-1}} \cdot f_k \cdot \nabla h(x - k\Delta x, t) \tag{6.8}$$

where the Grünwald weights f_k are given by:

$$f_k = \frac{\Gamma[k - (\alpha - 1)]}{\Gamma[-(\alpha - 1)]\Gamma[k + 1]} \tag{6.9}$$

where $\Gamma(\cdot)$ is the Γ function. Expression (6.9) means the following: for $k = 0$ we are at the last pixel of the steepest descent path, so $f_k = 1$. Then we read the previous location, update k, compute the corresponding weight f_k, update the sum and so forth until we have reached the upstream end of the upstream steepest path. Note that from every location in the field it is possible to trace more than one upstream path. In our simulations we have made the assumption that we compute the fractional derivative only along the longest upstream path. This assumption is acceptable in a system like the one simulated here, as the branching is fairly limited, due to the multiple outlets and the resulting configuration of the network constituted by several main stems with small tributaries.

6.4 Properties of the model at steady-state

In this section we compare steady-state landscapes resulting from the non-local model of (6.4) to those resulting from the nonlinear model (6.2) used in Passalacqua et al. [25]. We compare the steady-state landscapes in terms of appearance, slope-area relationship, cumulative area distribution and radial spectrum. The same metrics are reported for a real landscape, namely Coos Bay in Oregon.

Fig. 6.1 (a) shows a typical steady-state field obtained using the nonlinear model, while (b) shows the one obtained with the linear non-local model (6.4). Although the resulting landscape of the nonlinear model is less eroded than the one obtained with the linear non-local model (due to the strong grid resolution effect discussed by Passalacqua et al. [25]), the fluvial patterns created are very similar. The similarity among the two can be mostly appreciated in Fig. 6.2 (a) and (b), where the steady-state landscapes of Fig. 6.1 are shown on the (x, y) plane. We can notice how indistinguishable are the fluvial patterns created by the two models at steady state.

In addition to the appearance of the landscapes at steady-state, the time evolution observed during the numerical simulations has resulted similar. As reported in other works [86, 74, 69, 25], the time evolution of the landscape shows two different timescales:

a freezing time, corresponding to the channelization process, in which the river network reaches its final configuration, but the landscape is still eroded, and the relaxation time, corresponding to the maturation process, at which the landscape reaches its steady-state and erosion rate is in balance with uplift rate. These definitions are valid as long we consider a static steady-state, in which channels configuration does not change with time. While this is true in a numerical simulation, is not the case in nature, where continuous channels migration happen and the definition of steady-state has to be interpreted as a dynamic-steady-state condition.

Fig. 6.3 shows the cumulative area distributions $P(A)$ for (a) the steady-state field obtained from the nonlinear model (6.2), (b) the steady-state field obtained from the linear non-local model (6.4), and (c) Coos Bay, Oregon. The cumulative area distribution indicates the fraction of the landscape that has drainage area larger than a given A. On a log-log plot all the distribution show exponents in agreement with the ones found by other authors [84, 87, 86, 88, 73].

Fig. 6.4 shows the slope-area relationships for (a) the steady-state field obtained from the nonlinear model(6.2), (b) the steady-state field obtained from the linear non-local model (6.4), and (c) Coos Bay, Oregon. The nonlinear model shows an exponent ~ 0.5 as expected theoretically from (6.2) at steady state ($\partial_t h = 0$) and as observed also by the numerical results obtained by Somfai and Sander [73] with the same nonlinear model, while both the steady-state field obtained with (6.4) and Coos Bay show a lower value of the exponent. All the values are in the range reported in literature [78].

Fig. 6.5 shows the radial spectrum of (a) the steady-state field obtained from the nonlinear model(6.2), (b) the steady-state field obtained from the linear non-local model (6.4), and (c) Coos Bay, Oregon. The exponent of the radial spectrum offers a measure of the roughness and is equal to $-(2H + 2)$, where H is the Hurst exponent, which means a value of $H = 0.1$ for (a), $H = 0.4$ for (b) and $H = 0.35$ for (c).

We consider this analysis only the beginning of an effort to explore the merits, physical realism and physical interpretation of fractional transport laws for landscape evolution. It is noted that recent work by Baumer et al. [89] has opened up a new perspective for a physical interpretation of the model we proposed in (6.4). In particular, they showed that a fractional advection dispersion equation applied along flow paths is mathematically equivalent to an operation of subordination. Subordination means

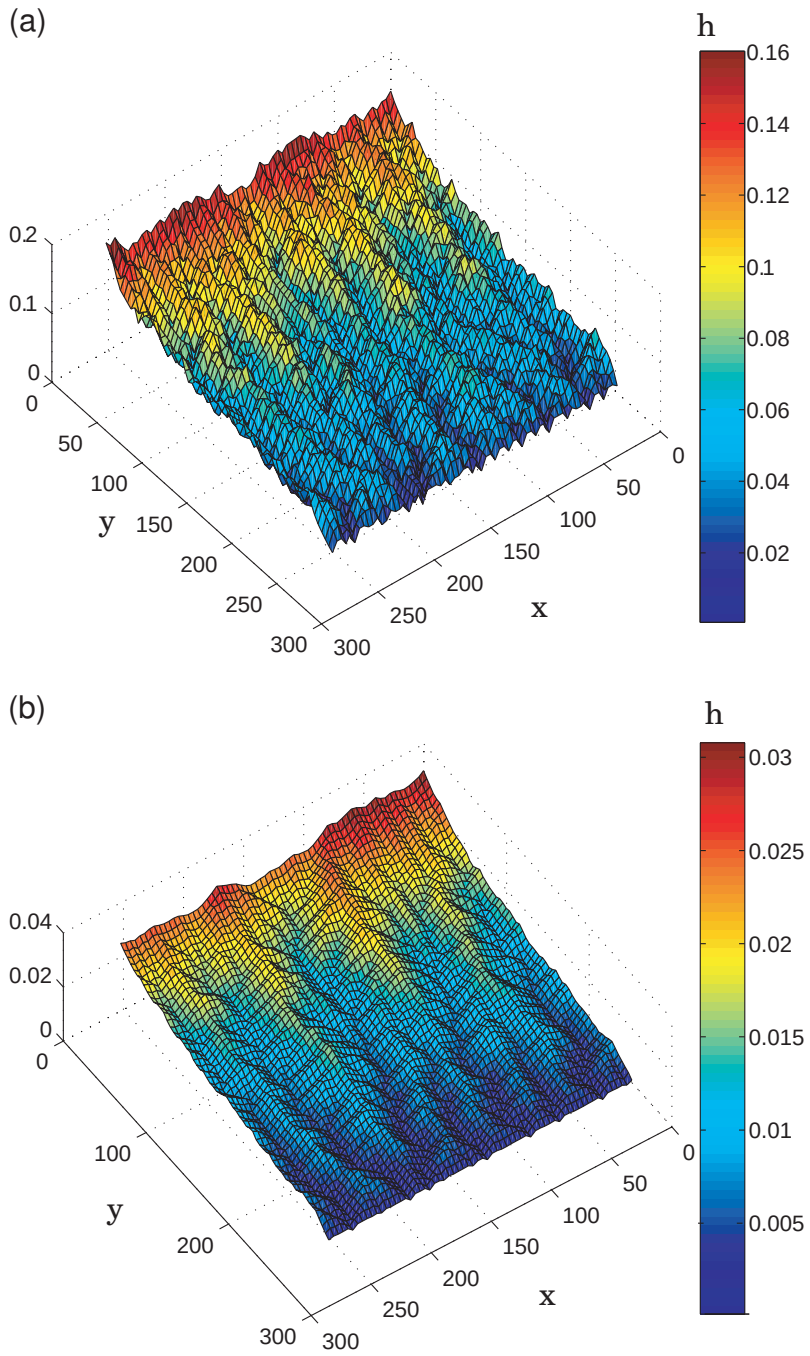

Figure 6.1: Steady-state field obtained using the nonlinear formulation (6.2) (a). Steady-state field obtained using equation (6.4) with the degree of nonlocality $\alpha = 1.5$ (b).

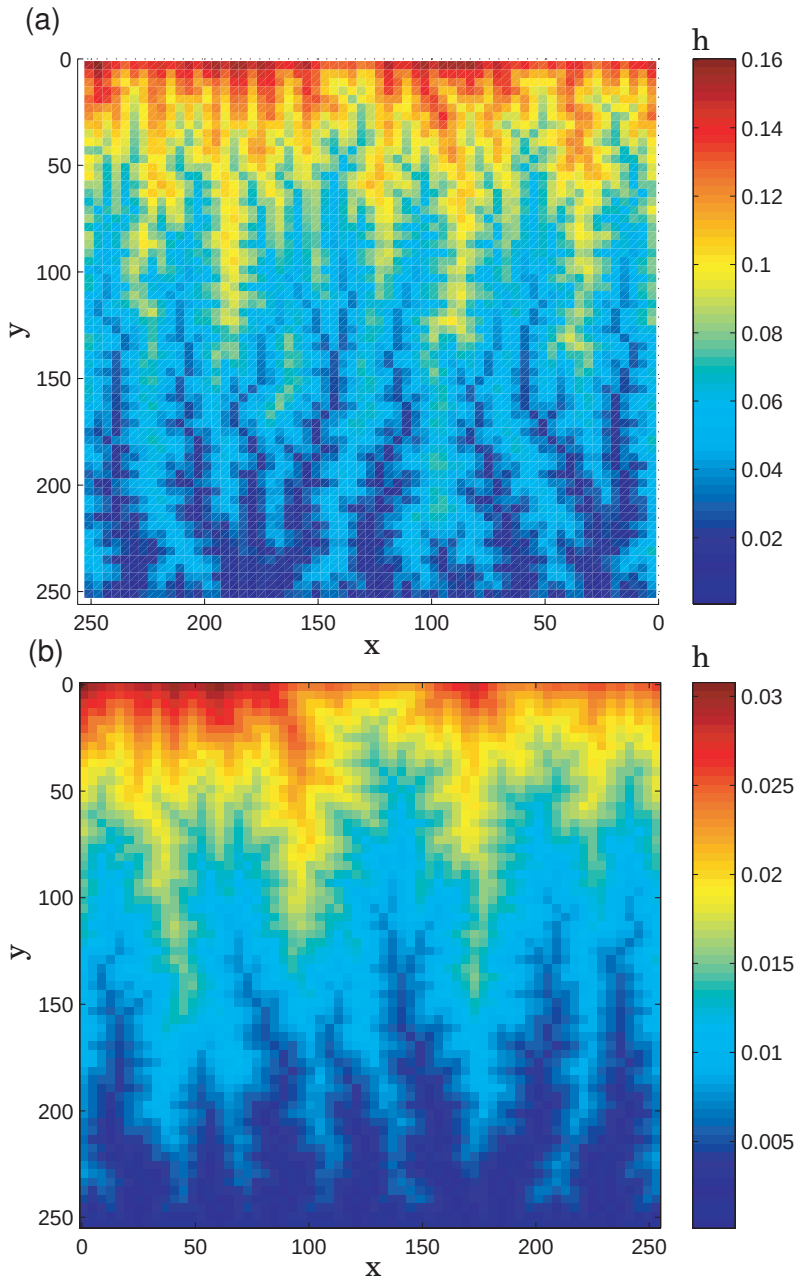

Figure 6.2: Steady-state field obtained using the nonlinear formulation (6.2) (a). Steady-state field obtained using equation (6.4) with the degree of nonlocality $\alpha = 1.5$ (b).

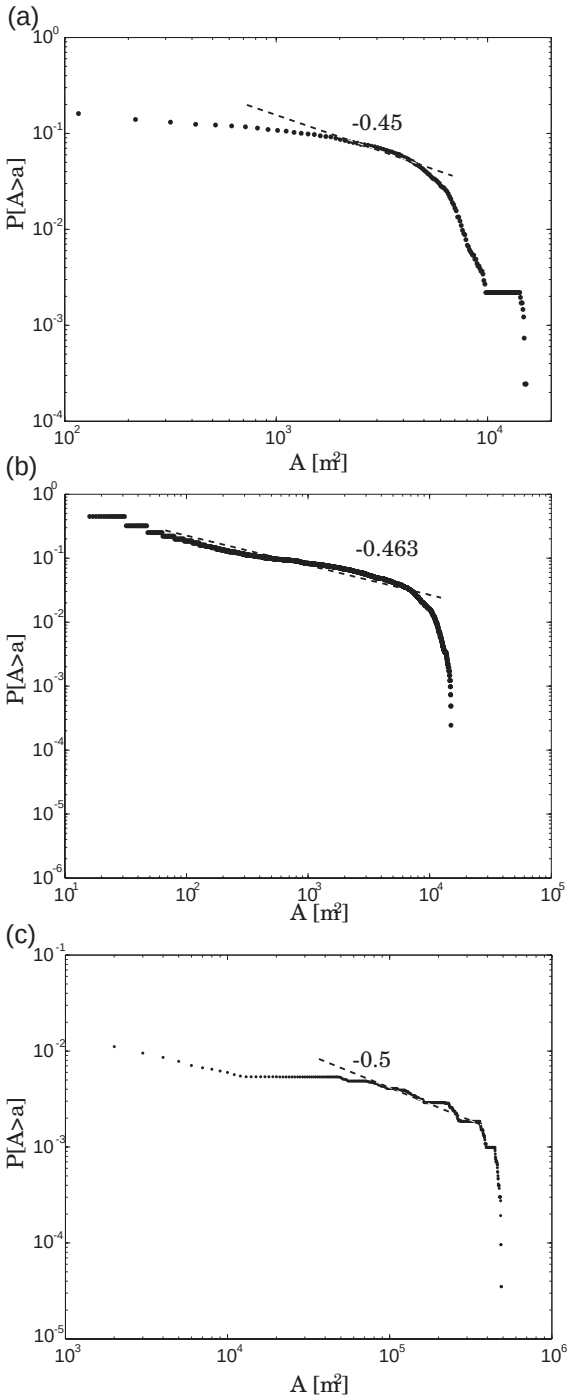

Figure 6.3: Cumulative area distribution for the field obtained from (6.2) at steady state (a). Cumulative area distribution for the field obtained from (6.4) at steady state (b). Cumulative area distribution for Coos Bay, Oregon (c).

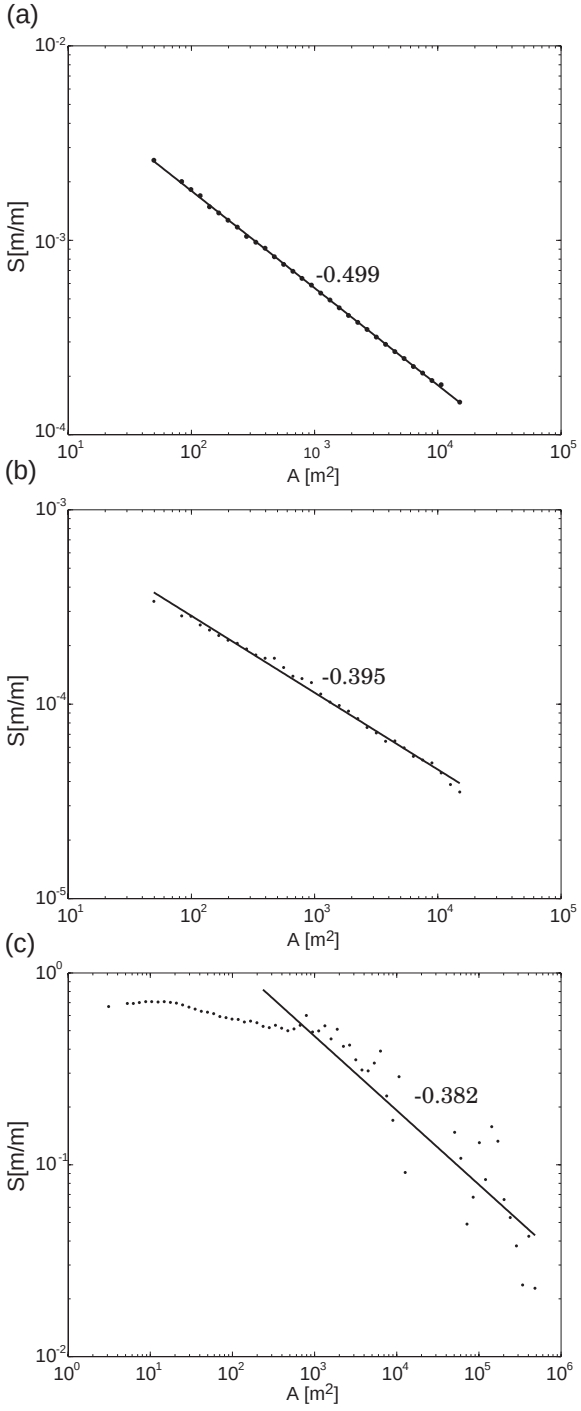

Figure 6.4: Relationship slope versus area for the steady-state field obtained using (6.2) (a). Relationship slope versus area for the steady-state field obtained using (6.4) (b). Relationship slope versus area obtained for Coos Bay, Oregon (c).

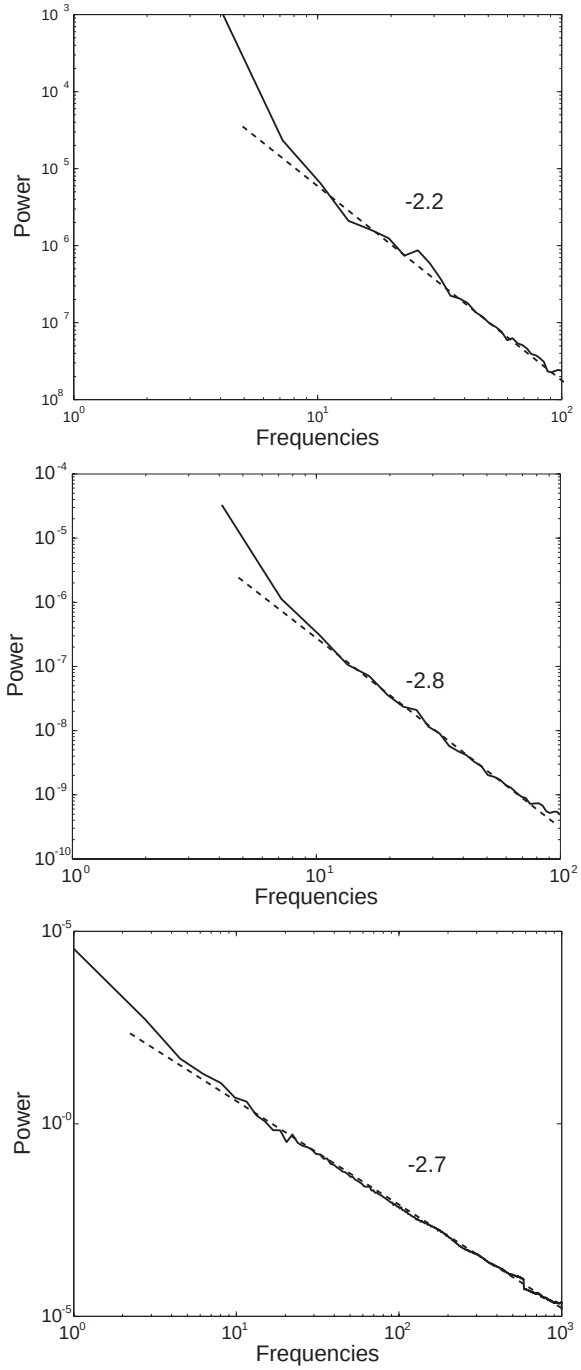

Figure 6.5: Radial spectrum of the steady-state field obtained from (6.2) (a).Radial spectrum of the steady-state field obtained from (6.4) (b). Radial spectrum of Coos Bay, Oregon (c).

that clock (actual) time is substituted with an 'operational time' which in our case would mimic the time at which erosion occurs, assuming a constant as opposed to a time-variable rate. In other words, variable in time erosion rate would be replaced by a constant erosion rate operating over a variable time (subordination). These concepts require further study and will form a direction for future research.

Chapter 7

Concluding Remarks and Future Perspectives

One of the contributions of this research is the development of a suite of multi-scale analysis methodologies for the efficient and automatic extraction of geomorphic features of interest from high resolution digital elevation data. We term this new research area as 'geomorphologically-informed image processing of landscapes' and foresee that it will occupy geomorphologists and earth-scientists considerably over the next decade as more and more high resolution topography (and vegetation) data become available from remote sensors to be used in process understanding and model building.

High resolution DEMs offer new opportunities for extracting detailed features from landscapes (e.g., channels, disruptions, channel heads, terraces, bluffs, ravines, etc.), but also challenges in developing extraction methodologies that are objective and computationally efficient. Space-scale representation methodologies used in image processing, have a lot to offer as they provide a framework within which one can achieve coarsening the landscape without smoothing out the features of interest, thus allowing the detection of those features efficiently.

In this work, we developed a methodology for geomorphic feature extraction which includes two main components: the pre-processing of the high resolution digital elevation data via nonlinear diffusion, to reduce noise and enhance features that are relevant to the network extraction, and the extraction of channel networks from the filtered data

via geodesic curves that incorporate geomorphologically-relevant information such as flow accumulation and curvature. The methodology (which is packaged under a toolbox called GeoNet) has been applied to three areas of very different characteristics: a steep and landslide-dissected basin, a mountainous basin and a flat region with natural and artificial features. Finally, it is compared to a previously proposed methodology based on wavelets.

The idea of approaching geomorphological analysis as a geometric task opens the door to many problems in the automatic extraction of information from LiDAR data. For the particular case of channel networks, it is important to study the possible benefits of using other nonlinear filtering methodologies for pre-processing as well as the introduction of additional features in the geodesic penalty function. Similarly, the exploitation of geomorphological analysis based on partial differential equations and variational formulations, which are popular in the image processing community, such as the Mumford-Shah functional [90], is of great interest for future research. For example, the channel networks can be considered as discontinuity fields and outliers, and as such be automatically computed by such an approach [91]. The feature extraction methodologies have been presented here for the case of a tributary system. However, with an appropriate modification of the cost function, they could also be applied to distributary or mixed systems, and this is an interesting direction for future research. Finally, the extraction of other geomorphic features, beyond those considered in this study such as landslides, debris flow regions, ravines, etc., is a subject for future research.

One motivation for extracting detailed geomorphic features from landscapes is the premise that this will lead to improved process understanding (e.g., by relating the observed form to physical processes that gave rise to that form) and improved modeling (e.g., by incorporating important localized features in hydrologic or sediment transport models or by developing sophisticated metrics for testing the performance of landscapes evolution models). With this premise in mind, work presented herein offers preliminary results along a particular new direction related to geomorphic transport laws and landscape evolution modeling. Specifically, motivated by: (a) our experience that geomorphic attributes, such as slope and curvature, are scale-dependent and thus the resulting sediment flux computed from the typical transport laws (e.g., linear Fickian

flux or nonlinear flux computation using the square of local slope) would also be scale-dependent, and (b) that landscapes present heterogeneity over a large range of scales, we put forward the idea of a non-local sediment flux formulation to be used in landscape evolution modeling. Along these lines, a simple landscape evolution model was proposed and its ability to reproduce some common statistical properties of real landscapes was examined.

The mathematical formulation of the proposed non-local landscape evolution model was based on a 2D fractional diffusion equation implemented via a time subordination on the flowpaths. The physical underpinning of the proposed model was briefly discussed but requires future elaboration. The results indicate that the proposed linear non-local model is able to reproduce a channelized fluvial landscape which mimics real ones (and also the ones produced by the commonly used Langevin-type local nonlinear model) in terms of slope-area relationships and scaling of contributing areas. Further work is required to fully explore the merits of this new class of non-local 2D sediment transport formulations for landscape evolution modeling and this presents a fruitful direction for future research.

References

[1] P. Perona and J. Malik. Scale-space and edge detection using anisotropic diffusion. *IEEE-PAMI*, 12:629–639, 1990.

[2] K. B. Gran, P. Belmont, S. S. Day, C. Jennings, A. Johnson, L. Perg, and P. R. Wilcock. Geomorphic evolution of the le sueur river, minnesota, usa, and implications for current sediment loading. In *Management and Restoration of Fluvial Systems with Broad Historical Changes and Human Impacts (edited by L. A. James, S. L. Rathburn, and G. R. Whittecar)*, pages XXX–XXX, doi:10.1130/2008.2451(08). Geology Society of America Special Paper 451, USA, 2009.

[3] W.E.H. Culling. Analytical theory of erosion. *J. Geol.*, 68:336–344, 1960.

[4] M.J. Kirkby. Hillslope process-response models based on the continuity equation. *Inst. Brit. Geogr., Spec. Publ.*, 3:15–30, 1971.

[5] T.R. Smith and F.P. Bretherton. Stability and the conservation of mass in drainage basin evolution. *Water Resour. Res.*, 8:1506–1529, 1972.

[6] F. Ahnert. Modelling landform change. In *Modelling Geomorphological Systems (edited by M.G. Anderson)*, pages 375–400. J. Wiley, London, 1988.

[7] G. Willgoose, R.L. Bras, and I. Rodriguez-Iturbe. A coupled channel network growth and hillslope evolution model; 1, theory. *Water Resour. Res.*, 27:1671–1684, 1991.

[8] G. Willgoose, R.L. Bras, and I. Rodriguez-Iturbe. A coupled channel network growth and hillslope evolution model; 2, nondimensionalization and application. *Water Resour. Res.*, 27:1685–1696, 1991.

[9] G. Willgoose, R.L. Bras, and I. Rodriguez-Iturbe. A physical explanation of an observed link area-slope relationship. *Water Resour. Res.*, 27:1697–1702, 1991.

[10] C. Chase. Fluvial landsculpting and the fractal dimension of topography. *Geomorphology*, 5:39–57, 1992.

[11] A. Rinaldo, W.E. Dietrich, R. Rigon, G.K. Vogel, and I. Rodriguez-Iturbe. Geomorphological signatures of climate. *Nature*, 374:632–635, 1995.

[12] A.D. Howard. Badlands. In *Geomorphology of Desert Environments (edited by A. D. Abrahams and A. J. Parsons)*, pages 213–242. Chapman and Hall, New York, 1994.

[13] A.D. Howard. A detachment-limited model of drainage basin evolution. *Water Resour. Res.*, 30 (7):2261–2285, 1994.

[14] R.S. Anderson. Evolution of the santa cruz mountains, california, through tectonic growth and geomorphic decay. *J. Geophys. Res.*, 99 (20):161–174, 1994.

[15] G. E. Tucker and R. L. Slingerland. Erosional dynamics, flexural isostacy, and long-lived escarpments: a numerical modeling study. *J. Geophys. Res.*, 99 (12):229–12–243, 1994.

[16] H. Kooi and C. Beaumont. Large-scale geomorphology; classical concepts reconciles and integrated with contemporary ideas via a surface processes model. *J. Geophys. Res.*, 101:3361–3386, 1996.

[17] I. Rodriguez-Iturbe and A. Rinaldo. *Fractal River Basins. Chance and Self-Organization.* Cambridge University Press, New York, 1997.

[18] T.R. Smith, B. Birnir, and G.E. Merchant. Towards an elementary theory of drainage basin evolution: I. the theoretical basis. *Comp. and Geosci.*, 23:811–822, 1997.

[19] T.R. Smith, B. Birnir, and G.E. Merchant. Towards an elementary theory of drainage basin evolution: Ii. a computational evaluation. *Comp. and Geosci.*, 23:823–849, 1997.

[20] G. E. Tucker and R. L. Slingerland. Drainage basin responses to climate change. *Water Resour. Res.*, 33:2031–2047, 1997.

[21] P. van der Beek and J. Braun. Controls on post-mid-cretaceous landscape evolution in the southeastern highlands of australia: Insights from numerical surface process models. *J. Geophys. Res.*, 104:4945–4966, 1999.

[22] G. E. Tucker and R. L. Bras. A stochastic approach to modeling the role of rainfall variability in drainage basin evolution. *Water Resour. Res.*, 36:1953–1964, 2000.

[23] W.E. Dietrich, D. Bellugi, A.M. Heimsath, J.J. Roering, L. Sklar, and J.D. Stock. Geomorphic transport laws for predicting landscape form and dynamics. In *Prediction in Geomorphology, Geophysical Monograph Series (edited by P. Wilcock and R. Iverson)*, pages 103–123. AGU, Washington D.C., 2003.

[24] C.P. Stark and G.J. Stark. A channelizataion model of landscape evolution. *Am. J. Sci.*, 301:486–512, 2001.

[25] P. Passalacqua, F. Porté-Agel, E. Foufoula-Georgiou, and C. Paola. Application of dynamic subgrid-scale concepts from large-eddy simulation to modeling landscape evolution. *Water Resour. Res.*, 42:W06D11, doi:10.1029/2006WR004879, 2006.

[26] B. Lashermes, E. Foufoula-Georgiou, and W. E. Dietrich. Channel network extraction from high resolution topography using wavelets. *Geophys. Res. Lett.*, 34:L23S04, doi:10.1029/2007GL031140, 2007.

[27] J. McKean and J. J. Roering. Objective landslide detection and surface morphology mapping using high-resolution airborne laser altimetry. *Geomorphology*, 57:331–351 doi:10.1016/S0169–555X(03)00164–8, 2004.

[28] N. F. Glenn, D. R. Streutker, D. J. Chadwick, G. D. Tahckray, and S. J. Dorsch. Analysis of lidar-derived topography information for characterizing and differentiating landslide morphology and activity. *Geomorphology*, 73:131–148, 2006.

[29] F. Ardizzone, M. Cardinali, M. Galli, F. Guzzetti, and P. Reichenbach. Identification and mapping of recent rainfall-induced landslides using elevation data collected by airborne lidar. *Nat. Hazards Earth Syst. Sci.*, 7 (6):637–650, 2007.

[30] A. Booth, J. J. Roering, and T. Perron. Automated landslide mapping using spectral analysis and high-resolution topographic data: Puget sound lowlands, washington, and portland hills, oregon. *Geomorphology*, 109:132–147, 2009.

[31] C. Gangodagamage, P. Belmont, and E. Foufoula-Georgiou. Statistical signature of deep-seated landslides. *J. Geophys. Res.*, under review, 2009.

[32] M. J. Smith, J. Rose, and S. Booth. Geomorphological mapping of glacial landforms from remotely sensed data: an evaluation of the principal data sources and an assessment of their quality. *Geomorphology*, 76:148–165 doi:10.1016/j.geomorph.2005.11.001, 2006.

[33] D. M. Staley, T. A. Wasklewicz, and J. S. Blaszczynski. Surficial patterns of debris flow deposition on alluvial fans in death valley, ca using airborne laser swath mapping. *Geomorphology*, 74:152–163, 2006.

[34] K. L. Frankel and J. F. Dolan. Characterizing arid region alluvial fan surface roughness with airborne laser swath mapping digital topographic data. *J. Geophys. Res.*, 112:F02025 doi:10.1029/2006JF000644, 2007.

[35] M. Cavalli and L. Marchi. Characterization of the surface morphology of an alpine alluvial fan using airborne lidar. *Nat. Hazards Earth Syst. Sci.*, 8:323–333, 2007.

[36] M. Cavalli, P. Tarolli, L. Marchi, and G. Dalla Fontana. The effectiveness of airborne lidar data in the recognition of channel bed morphology. *Catena*, 73:249–260 doi:1016/j.catena.2007.11.001, 2008.

[37] A. Vianello, M. Cavalli, and P. Tarolli. Lidar-derived slopes for headwater channel network analysis. *Catena*, 76:97–106 doi:10.1016/j.catena.2008.09.012, 2009.

[38] J. Koenderink. The structure of images. *Biol. Cybern.*, 50:363–370, 1984.

[39] F. Catté, P. L. Lions, J. M. Morel, and T. Coll. Image selective smoothing and edge detection by nonlinear diffusion. *SIAM J. Numer. Anal.*, 29 (1):182–193, 1992.

[40] L. Alvarez, P. L. Lions, and J. M. Morel. Image selective smoothing and edge detection by nonlinear diffusion. *SIAM J. Numer. Anal.*, 29 (3):845–866, 1992.

[41] M.P. Do Carmo. *Differential Geometry of Curves and Surfaces*. Prentice Hall, New Jersey, 1976.

[42] L. Yatziv, A. Bartesaghi, and G. Sapiro. O(n) implementation of the fast marching algorithm. *Journal of Computational Physics*, 212:393–399, 2006.

[43] R.B. Dial. Algorithm 360: Shortest-path forest with topological ordering. *Communications of the ACM*, 12, 1969.

[44] E. Dijkstra. A note on two problems in connection with graphs. *Numerische Math.*, 1:269–271, 1959.

[45] R. Kimmel. *Numerical Geometry of Images: Theory, Algorithms, and Applications*. Springer, New York, 2003.

[46] F. Memoli and G. Sapiro. Distance functions and geodesics on submanifolds of r^d and point clouds. *SIAM Journal Applied Math.*, 65:1227–1260, 2005.

[47] J. Helmsen, E.G. Puckett, P. Collela, and M. Dorr. Two new methods for simulating photolithography development in 3d. *Proc. SPIE microlithology*, IX:253, 1996.

[48] J. Sethian. *Level Set Methods and Fast Marching Methods*. Cambridge University Press, Cambridge, UK, 1999.

[49] J. N. Tsitsiklis. Efficient algorithms for globally optimal trajectories. *IEEE Transactions on Automatic Control*, 40:1528–1538, 1995.

[50] Y. R. Tsai, L. T. Cheng, S. Osher, and H. K. Zhao. Fast sweeping algorithms for a class of hamilton-jacobi equations. *SIAM Journal on Numerical Analysis*, 41(2):673–694, 2003.

[51] H.K. Zhao. Fast sweeping method for eikonal equations. *Mathematics of Computation*, 74:603–627, 2004.

[52] S. Mallat. *A Wavelet Tour of Signal Processing*. Academic Press, San Diego, CA, 1998.

[53] P. Kumar and E. Foufoula-Georgiou. Wavelet analysis for geophysical applications. *Rev. in Geophysics*, 35(4):385–412, 1997.

[54] M. Black, G. Sapiro, D. Marimont, and D. Heeger. Robust anisotropic diffusion. *IEEE T. Image Process.*, 7 (3):421–432, 1998.

[55] D. G. Tarboton. A new method for the determination of flow directions and contributing areas in grid digital elevation models. *Water Resour. Res.*, 33 (2):309–319, 1997.

[56] P. Passalacqua, T. Do Trung, E. Foufoula-Georgiou, G. Sapiro, and W. E. Dietrich. A geometric framework for channel network extraction from lidar: nonlinear diffusion and geodesic paths. *J. Geophys. Res.*, in press, 2009.

[57] M. Lenzi. Step-pool evolution in the rio cordon, northeastern italy. *Earth Surf. Proc. Land.*, 26:991–1008, 2001.

[58] M. Lenzi, L. Mao, and F. Comiti. Magnitude-frequency analysis of bed load data in an alpine boulder bed stream. *Water Res. Resour.*, 40:W07201 doi:10.1029/2003WR002961, 2004.

[59] P. Tarolli, M. Borga, and G. Dalla Fontana. Analyzing the influence of upslope bedrock outcrops on shallow landsliding. *Geomorphology*, 93:186–200 doi:10.1016/j.geomorph.2007.02.017, 2008.

[60] W. E. Dietrich and T. Dunne. The channel head. In *Channel Network Hydrology (edited by K. Bevan and M. J. Kirkby)*, pages 175–219. Wiley, Chichester, 1993.

[61] D. R. Montgomery and J. M. Buffington. Channel-reach morphology in mountain drainage basins. *Geol. Soc. Am. Bull.*, 109 (5):596–611, 1997.

[62] D. R. Montgomery and W. E. Dietrich. Channel initiation, drainage density and slope. *Water Resour. Res.*, 25 (8):1907–1918, 1989.

[63] A. Vianello and V. D'Agostino. Bankfull width and morphological units in an alpine stream of the dolomites (northern italy). *Geomorphology*, 83:266–281 doi:10.1016/j.geomorph.2006.02.023, 2007.

[64] P. Tarolli and G. Dalla Fontana. Hillslope to valley transition morphology: new opportunities from high resolution dtms. *Geomorphology*, in press:doi:10.1016/j.geomorph.2009.02.006, 2009.

[65] E. Foufoula-Georgiou, V. Ganti, and W. E. Dietrich. A non-local theory for sediment transport on hillslopes. *J. Geophys. Res.*, under review, 2009.

[66] G. E. Tucker and D. N. Bradley. The trouble with diffusion: reassessing hillslope erosion laws with a particle-based model. *J. Geophys. Res.*, in press:doi:10.1029/2009JF001264, 2009.

[67] L. Benda and T. Dunne. Stochastic forcing of sediment supply to channel networks from landsliding and debris flow. *Water Resour. Res.*, 33 (12):2849–2863, 1997.

[68] L. Benda and T. Dunne. Stochastic forcing of sediment routing and storage in channel networks. *Water Resour. Res.*, 33 (12):2865–2880, 1997.

[69] B. Birnir, T. R. Smith, and G. E. Merchant. The scaling of fluvial landscapes. *Comp. Geosci.*, 27:1189–1216, 2001.

[70] J.J. Roering. How well can hillslope evolution models 'explain' topography? simulating soil transport and production with high-reolution topographic data. *Geol. Soc. Am. Bull.*, 120 (9):1248–1262, 2008.

[71] M. Kardar, G. Parisi, and Y.-C. Zhang. Dynamic scaling of growing interfaces. *Phys. Rev. Lett.*, 56:889–892, 1986.

[72] D. Sornette and Y.C. Zhang. Non linear langevin model of geomorphic erosion processes. *Geophys. J. Int.*, 113:382–386, 1993.

[73] E. Somfai and L.M. Sander. Scaling and river networks-a landau theory for erosion. *Phys. Rev. E*, 56:R5–R8, 1997.

[74] J. R. Banavar, F. Colaiori, A. Flammini, A. Maritan, and A. Rinaldo. Scaling, optimality and landscape evolution. *J. Stat. Phys.*, 104:1–49, 2001.

[75] K.X. Whipple and G.E. Tucker. Dynamics of the stream-power river incision model: Implications for height limits of mountain ranges, landscape response timescales, and research needs. *J. Geophys. Res.*, 104 (17):661–674, 1999.

[76] N. P. Snyder, K. X. Whipple, G. E. Tucker, and D. J. Merritts. Landscape response to tectonic forcing: digital elevation model analysis of stream profiles in the mendocino triple junction region, northern california. *Geol. Soc. Am. Bull.*, 112:1250–1263, 2000.

[77] E. Kirkby and K. Whipple. Quantifying differential rock-uplift rates via stream profile analysis. *Geology*, 29:415–418, 2001.

[78] K.X. Whipple and G.E. Tucker. Implications of sedimentflux-dependent river incision models for landscape evolution. *J. Geophys. Res.*, 107, NO. B2:doi:10.1029/2000JB000044, 2002.

[79] K. Miller and B. Ross. *Introduction to the Fractional Calculus and Fractional Differential Equations*. John Wiley and Sons, New York, 1993.

[80] R. Schumer, M. M. Meerschaert, and B. Baeumer. What are fractional advection-dispersion equations? *J. Geophys. Res.*, in press, 2009.

[81] J. T. Hack. Interpretation of erosional topography in humid temperate regions. *Am. J. Sci.*, 258 A:80–97, 1960.

[82] J.Adams. Contemporary uplift and erosion of southern alps, new zealand: Summary. *Geol. Soc. Am. Bull.*, 91:2–4, 1980.

[83] S. D. Willett and M. T. Brandon. On steady states in mountain belts. *Geology*, 30:175–178, 2002.

[84] H. Inaoka and H. Takayasu. Water erosion as a fractal growth process. *Phys. Rev. E*, 47:899–910, 1993.

[85] A. K. Grünwald. Uber 'begrenzt' derivationen und deren anwendung. *Z. angew. Math. und Phys.*, 12:441–480, 1867.

[86] K. Sinclair and R. C. Ball. Mechanism for global optimization of river networks from local erosion rules. *Phys. Rev. Lett.*, 76:3360–3363, 1996.

[87] A. Rinaldo, A. Maritan, F. Colaiori, A. Flammini, R. Rigon, I. Rodriguez-Iturbe, and J. R. Banavar. Thermodynamics of fractal networks. *Phys. Rev. Lett.*, 76:3364–3367, 1996.

[88] J. R. Banavar, F. Colaiori, A. Flammini, A. Giacometti, A. Maritan, and A. Rinaldo. Sculpting of a fractal river basin. *Phys. Rev. Lett.*, 78 (23):4522–4525, 1997.

[89] B. Baumer, M. Haase, and M. Kovács. Unbounded functional calculus for bounded groups with applications. *J. Evol. Equ.*, 9:171–195, 2009.

[90] D. Mumford and J. Shah. Optimal approximation by piecewise smooth functions and associated variational problems. *Commun. Pur. Appl. Math.*, XLII:577–685, 1989.

[91] G. Sapiro. *Geometric Partial Differential Equations and Image Analysis.* Ralph M. Parson Lab., Dept. of Civil Engineering MIT, Cambridge, Mass., 1989.